Atomistic Simulations of 40 Ar Diffusion in Muscovite

Jehiel Nteme, Stéphane Scaillet, Pascal Brault, Laurent Tassan-Got

Journal Pre-proofs

Atomistic Simulations of 40 Ar Diffusion in Muscovite

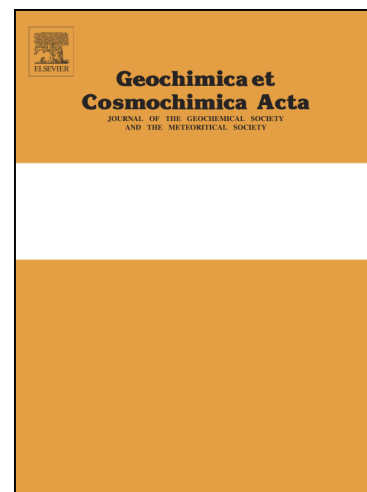Jehiel Nteme, Stéphane Scaillet, Pascal Brault, Laurent Tassan-Got

Click here to view linked References ⬇

Atomistic Simulations of ^{40}Ar Diffusion in Muscovite

Jehiel Nteme[a,b,*], Stéphane Scaillet[a], Pascal Brault[b], Laurent Tassan-Got[c,d]

[a]*Univ. Orléans, CNRS, BRGM, Institut des Sciences de la Terre d'Orléans (ISTO), UMR 7327, F-45071, Orléans, France*
[b]*Univ. Orléans, CNRS, Groupe de Recherches sur l'Energétique des Milieux Ionisés (GREMI), UMR 7344, 45067 Orléans, France*
[c]*Université Paris-Saclay, CNRS, IN2P3, Laboratoire de Physique des deux infinis Irène Joliot-Curie (IJCLab), 91405 Orsay, France*
[d]*Conseil Européen pour la Recherche Nucléaire (CERN), Espl. des Particules 1, 1211 Meyrin, Geneva, Switzerland*

Abstract

Muscovite ranks among the most commonly dated minerals in ^{40}Ar/^{39}Ar geochronology. Yet, its use in thermochronological reconstructions is hampered by the lack of reliable data on its ^{40}Ar diffusional behavior. In this contribution, we investigate ^{40}Ar lattice diffusion in muscovite at the atomic scale using Molecular Dynamics (MD) simulations combined with Nudged Elastic Band (NEB) and Transition State Theory (TST). Classical MD simulations of ^{40}Ar recoil dynamics in $2M_1$ muscovite reveal that ^{40}Ar initially resides predominantly in the interlayer region, close to its production site. Systematic computations of migration barriers coupling NEB with TST identify the divacancy mechanism as the more energetically favorable pathway for ^{40}Ar diffusion in the interlayer region, with characteristic enthalpy of motion $E = 66$ kcal.mol^{-1} and vibrational entropy term $D_0 = 6 \times 10^{-4}$ cm^2.s^{-1}. For typical cooling rates between $1-100$ °C.Ma^{-1} and grain size varying from 0.1 and 1 mm, these parameters predict closure temperatures significantly higher (~ 200 °C) than currently accepted maximum estimates (~ 500 °C). Consistent with long-standing empirical evidence, our theoretical results downplay the role of purely thermally activated diffusion in promoting efficient ^{40}Ar transport in ideal (stoichiometrically stable and undefective) muscovite. Along with experimental and field-based evidence, they call for more complex physics to explain the ^{40}Ar retention properties of natural muscovite, most notably by considering crystal-chemical disequilibrium interactions and the reactivity of the interlayer with the external medium.

Keywords: ^{40}Ar diffusion, Muscovite, Molecular Dynamics, Transition State Theory, Thermochronology

---

*Corresponding author
Email address:* `jehiel.nteme-mukonzo@univ-orleans.fr` (Jehiel Nteme)

1. Introduction

Diffusion is the main mechanism governing atomic transport in minerals. It is fundamental to the understanding of many geological processes in terms of kinetics of metamorphic transformations and closure behavior of radio-isotopic systems (Dodson, 1973). Among these, the ^{40}Ar/^{39}Ar dating technique has been widely applied for studying Earth processes in the thermal range controlling the retention behavior of ^{40}Ar$-$bearing minerals (McDougall and Harrison, 1999). Being non bonded, ^{40}Ar is expected to be much more mobile than silicate-forming elements and therefore much more sensitive to thermal effects. The commonly observed discordance between for example ^{40}Ar/^{39}Ar and U/Pb ages has been attributed to the fact that common minerals lose their ^{40}Ar at crustal medium to moderate temperatures, giving apparent ^{40}Ar/^{39}Ar ages that do not reflect the time of crystallization but the time when the mineral was sufficiently cold to become effectively closed to ^{40}Ar loss by diffusion (Hart, 1960; Armstrong, 1966). Such a closed-system behavior has been theoretized in terms of a physically defined closure temperature (T_c) taking into account the Arrhenian dependence of intracrystalline (lattice) diffusion to temperature according to (Dodson, 1973):

$$T_c = \frac{E}{R \ln \left(\dfrac{A R T_c^2 \, D_0/a^2}{E \, dT/dt} \right)} \tag{1}$$

in which E is the activation energy and D_0 the pre-exponential factor. dT/dt is the cooling rate, a the diffusion radius, A a numerical constant appropriate for the chosen geometry for diffusion, and R the gas constant. This expression emphasizes the importance of the diffusion parameters E and D_o in any quantitative interpretation of ^{40}Ar/^{39}Ar metamorphic ages in terms of thermal-kinetic crustal processes.

Among those minerals commonly dated by ^{40}Ar/^{39}Ar, muscovite stands apart due to its high potassium content and ubiquity in most crustal lithologies, all the way down from the epizone to subduction-zone metamorphic conditions (McDougall and Harrison, 1999). However, the ^{40}Ar diffusion behavior in muscovite remains poorly understood. Early on, maximum retention temperatures of ca. 350 °C to as high as 400 °C (or greater) were inferred from field calibration of apparent ages vs. metamorphic grade (Purdy and Jäger, 1976)

2

and pioneering diffusion experiments (Hart, 1960). Other ^{40}Ar diffusivity estimates were later proposed by Hames and Bowring (1994), Lister and Baldwin (1996) and Kirschner et al. (1996). Hames and Bowring (1994) and Lister and Baldwin (1996) re-evaluated the early thermal-hydrothermal experimental data of Robbins (1972) to suggest the values $E = 52$ kcal.mol^{-1} and $D_0 = 0.04$ cm^2.s^{-1} (Hames and Bowring, 1994), and $E = 41.8$ kcal.mol^{-1} and $D_0 = 3.352 \times 10^{-7}$ cm^2.s^{-1} (Lister and Baldwin, 1996). Kirschner et al. (1996) inferred an activation energy of $E = 58$ kcal.mol^{-1} with $D_0 = 0.24$ cm^2.s^{-1} from an empirical thermal model binned to ^{40}Ar/^{39}Ar ages in muscovites grown during nappe thrusting in the Western Alps. Nowadays, commonly adopted values are those determined by Harrison et al. (2009) from hydrothermal experiments conducted in the range 730-600 °C and $P = 10$, 20 kbar ($E = 63$ kcal.mol^{-1}; $D_0 = 2.3$ cm^2.s^{-1}). Some other estimates were inferred by Forster and Lister (2014) and Lister and Forster (2016) using in vacuo experiments ($E = 67$ kcal.mol^{-1} and $D_0/a^2 = 1.2 \times 10^9$ s^{-1}).

These parameters imply theoretical ^{40}Ar-closure temperatures lower than 500 °C (Harrison et al. 2009). However, cases of effective ^{40}Ar retention have been consistently reported for muscovites exposed to temperatures in excess of this value (Monié, 1990; Scaillet et al., 1990, 1992; Monié and Chopin, 1991; Arnaud and Kelley, 1995; Scaillet, 1996; Di Vincenzo et al., 2001, 2004, 2006; Balogh and Dunkl, 2005; Hames et al., 2008; Itaya et al., 2009; Allaz et al., 2011; Beltrando et al., 2013; Halama et al., 2014; Schertl and Hammerschmidt, 2016; Laurent et al., 2021). While most of these studies relate to high-pressure phengites from eclogite-facies rocks for which the combined effect of pressure and composition (e.g., Tschermak substitution) may have influenced the ^{40}Ar diffusion behavior (Wijbrans and Mcdougall, 1986; Scaillet et al., 1992; Scaillet, 1998), a high retentivity has also been suggested in other settings for which compositional and pressure effects are not prevalent (Di Vincenzo et al., 2004; Hames et al., 2008; Itaya et al., 2009; Allaz et al., 2011). The discordance between experimental predictions and geologic evidence raises the fundamental question as to the meaning of such ^{40}Ar/^{39}Ar ages: Do they reflect cooling or (re)crystallization? The answer requires a better understanding of the ^{40}Ar diffusion behavior in muscovite as a function of several parameters including temperature, chemical composition, and other intensive variables such as pressure.

3

In this work, we focus on the ^{40}Ar diffusional behavior in muscovite with respect to temperature. Unlike previous studies that investigated the ^{40}Ar diffusivity in muscovite experimentally and empirically, we re-evaluate the ^{40}Ar diffusion dependence to temperature via atomistic simulations. These simulations, which include various methods (e.g., Density Functional Theory − DFT, Molecular Dynamics − MD, Kinetic Monte-Carlo − KMC, etc.), show many advantages over laboratory experiments. While the determination of rare-gas diffusivities in hydrothermal experiments is based on finite-state observables (fractional loss), atomistic simulations investigate the diffusion behavior at the atomic scale, allowing the identification and characterization of the diffusion mechanism (e.g., interstitial vs. vacancy mechanism) apt to explain the bulk migration of the diffusing species across the crystal. Also, atomistic simulations permit to analyze the diffusion process in a perfect lattice structure, unlike laboratory experiments that use natural crystals which commonly contain impurities and microstructural defects.

Atomistic simulations have been widely applied to the study of solid-state diffusion in the field of Material Science. Quite recently, they have been used for the theoretical characterization of low-temperature (fast-diffusing) thermochronometers like He and Ne in hematite, goethite, zircon, apatite and quartz via a multi-scale approach combining DFT with KMC (Saadoune et al., 2009; Bengston et al., 2012; Djimbi et al., 2015; Balout et al., 2017a,b; Gerin et al., 2017; Bassal et al., 2020; Domingos et al., 2020; Gautheron et al., 2020). DFT simulations of rare-gas (He, Ne, Ar, Kr, Xe) diffusion in hydrated minerals have further been applied to quantify the efficiency of noble gas recycling in subduction zones (Wang et al., 2020). DFT has also been successfully used to constrain He diffusion in olivine, quartz and coesite at mantle pressures (Wang et al., 2015; Liu et al., 2021). In this paper, we investigate ^{40}Ar diffusion in muscovite by combining MD with TST. Our results reveal ^{40}Ar diffusion kinetics several orders of magnitude slower than current estimates.

2. Methods

2.1. Crystal structure model

The crystal structure of muscovite [$KAl_2(Si_3Al)O_{10}(OH)_2$] consists of a stacking of tetrahedral - octahedral - tetrahedral (T−O−T) layers held together across the interlayer space

4

118 by K^+ ions, which compensate the negative structural charge resulting from the substitution

119 of Al for Si (Bailey, 1984). Tetrahedral silicon layers and dioctahedral aluminum layers are

120 connected through bridging oxygens. In this work, we use a $2M_1$ muscovite atomic model

121 based on the structural data of Catti et al. (1989). The model consists of a periodic supercell

122 of $6 \times 3 \times 1$ unit cells along the crystallographic directions a, b, and c, respectively (Fig. 1a).

123 Tetrahedral Al atoms are distributed in an irregular pattern while obeying the short range

124 Lowenstein rule (Loewenstein, 1954) and the principle of local charge balance (Herrero et

125 al., 1985, 1987). Accordingly, no $^{IV}Al-O-^{IV}Al$ bond was allowed and each hexagonal tetra-

126 hedral ring contains either one or two Al atoms (Fig. 1b). Each K^+ is located between one

127 Si_4Al_2 ring and one Si_5Al_1 ring to ensure an equitable charge distribution.

128 2.2. Computational details

129 Classical Molecular dynamics (MD) consists in simulating the trajectory of a system of

130 interacting particles (atoms and/or molecules) over time by solving Newton's equations of

131 motion (Frenkel and Smith, 2002; Rapaport, 2004). Interatomic interactions are computed

132 based on force fields, which are parameterized using experimental results or *ab initio* simu-

133 lations. We performed MD simulations using the simulation package LAMMPS (Thompson

134 et al., 2021). The interatomic interactions were computed using ClayFF, a non-reactive

135 force field that describes hydrated mineral systems through essentially nonbonded potentials

136 (Cygan et al., 2004). Since its development, this force field has been widely used in MD

137 simulations of phyllosilicates and other common minerals for which it has been shown to

138 faithfully reproduce the structure and many thermodynamic properties (Greathouse et al.,

139 2005, 2006; Kirkpatrick et al., 2005; Padma et al., 2006; Larentzos et al., 2007; Liu et al.,

140 2007, 2008; Kerisit et al., 2008; Meleshyn, 2008; Wander and Clark, 2008; Cygan et al., 2009;

141 Malani et al., 2009; Ferrage et al., 2010; Kalinichev et al., 2010; Tao et al., 2010; Argyris

142 et al., 2011a,b; Ho et al., 2011; Teich-McGoldrick et al., 2012; Churakov, 2013; Loganathan

143 and Kalinichev, 2013; Morrow et al., 2013). The pairwise energy for atoms i and j separated

144 by a distance r_{ij} is given by

$$145 \qquad E_{ij} = \frac{e^2 q_i q_j}{4\pi\epsilon_0 r_{ij}} + 4\epsilon_{ij}\left[\left(\frac{\sigma_{ij}}{r_{ij}}\right)^{12} - \left(\frac{\sigma_{ij}}{r_{ij}}\right)^6\right] \qquad (2)$$

146 where e is the fundamental charge of an electron, q_i and q_j are partial atomic charges and ϵ_0
147 is the permittivity of vacuum. The Lennard-Jones parameters σ_{ij} and ϵ_{ij} correspond to the
148 zero-crossing distance for the energy and the depth of the potential energy well, respectively.
149 Interaction between hydroxyl atoms are computed with a bonded potential that describes
150 the bond stretch energy by a simple harmonic term:

$$E_{ij}^{\text{bond}} = k_1(r_{ij} - r_0)^2 \tag{3}$$

152 where k_1 is a force constant and r_0 the equilibrium bond length. Interaction parameters
153 used in this study are provided in Table 1. As there are no parameters for Ar in ClayFF,
154 we assigned it a zero charge and Lennard-Jones parameters as reported by White (1999).
155 The nonbonded parameters are given for interactions between identical atom types ($i =$
156 j). Interaction parameters between unlike atoms ($i \neq j$) are calculated using the Lorentz-
157 Berthelot mixing rules:

$$\sigma_{ij} = \frac{1}{2}(\sigma_i + \sigma_j) \tag{4}$$

$$\epsilon_{ij} = \sqrt{\epsilon_i \epsilon_j} \tag{5}$$

162 The muscovite atomic model was optimized in a series of preliminary calculations consist-
163 ing of energy minimization followed by 250 ps MD runs performed in the isobaric-isothermal
164 (NPT) ensemble using the Nosé-Hoover thermostat and barostat, with damping parameters
165 for temperature and pressure of 0.01 and 1 ps, respectively, and a time step of 0.001 ps.
166 Short-range interactions were evaluated with a cut-off distance of 10 Å whereas long-range
167 interactions were treated using the Ewald summation. The ^{40}Ar diffusion energy barriers
168 were quantified using the Nudged Elastic Band (NEB) method (Jónsson et al., 1998), which
169 determines the minimum energy path (MEP) between two stable sites by solving simultane-
170 ously independent system images, each one containing one ^{40}Ar atom located on the path
171 connecting the stable sites. Images are linked by a spring force to ensure the continuity of
172 the path and the equal spacing between images along the MEP. The migration energy is
173 obtained by taking the difference in energy between the saddle point and the initial stable
174 site. In this study, eight images were generated and all the NEB calculations were performed
175 with a spring constant of 23 kcal.mol^{-1}.Å^{-2}.

The transport rate based on those migration barriers was evaluated using the Transition State Theory (TST) that expresses the jump probability γ as:

$$\gamma = \nu \exp\left(\frac{-E}{RT}\right) \tag{6}$$

where ν is the attempt frequency, E the migration barrier, R the gas constant, and T the temperature of the system (in Kelvin). The attempt frequency is given by:

$$\nu = \frac{\displaystyle\prod_{i=1}^{3N} \nu_i^{init}}{\displaystyle\prod_{i=1}^{3N-1} \nu_i^*} \tag{7}$$

in which ν_i^{init} corresponds to the modal vibrational frequencies at the stable site and ν_i^* represents the non-imaginary modal frequencies at the saddle point (Vineyard, 1957). For most solids, the attempt frequency is comprised between 10^{12} s^{-1} and 10^{13} s^{-1}. This parameter is usually approximated by a fixed value within this interval to avoid the computationally expensive determination of modal frequencies. In this work, we used $\nu = 5 \times 10^{12}$ s^{-1}, which is close to the attempt frequency of 4.61×10^{12} s^{-1} computed via DFT for Ar in lizardite (Wang et al., 2020). The diffusion coefficient is related to the transition rate via:

$$D = ga^2\gamma = ga^2\nu \exp\left(\frac{-E}{RT}\right) \tag{8}$$

where g is a numerical constant depending on the geometry of the lattice and a is the distance between two neighboring stable sites. The frequency factor D_0 is given by:

$$D_0 = ga^2\nu \tag{9}$$

3. Force field validation

To validate the application of the ClayFF force field to the study of muscovite, we compared the lattice parameters computed at ambient conditions ($P = 0.001$ kbar and $T = 25$ °C) for our muscovite atomic model with experimental data (Catti et al., 1989). The results (Table 2) show that ClayFF reproduces the experimental crystal structure well. The lattice parameters a, b, c and the angles α, β, γ are all within 2 % (and in most cases 0.5 %)

7

199 of the experimental values. The interlayer separation is also well reproduced (within 1 % of
200 experimental determinations). Moreover, ClayFF also faithfully reproduces the stacking of
201 adjacent T−O−T layers. In the interlayer region, the basal oxygens of one T−O−T layer
202 are directly above those of the adjacent layer, in keeping with experimental determinations.
203 Each potassium atom is located at the center of the upper and lower tetrahedral rings. As
204 expected for a di-octahedral mica, the hydroxyl groups point towards the vacant octahedral
205 site and remain subparallel to the (001) plane.

4. ^{40}Ar initial position from interlayer recoil dynamics

207 The investigation of ^{40}Ar diffusion at the atomic scale requires the determination of its
208 insertion site within the muscovite structure. Since ^{40}Ar is produced with a kinetic energy
209 of 660 kcal.mol^{-1} corresponding to a velocity of 0.11765 Å.fs^{-1} (Dong et al., 1995; Szczerba
210 et al., 2015), the ^{40}Ar insertion site can be determined by modelling the natural ^{40}Ar recoil
211 via MD simulations. Such simulations have been performed by Szczerba et al. (2015), who
212 investigated the natural recoil of ^{40}Ar in illite, a clay mineral structurally similar to muscovite.
213 Using both REAXFF and ClayFF force fields, they performed several simulations in which
214 ^{40}Ar had the same initial velocity (0.11765 Å.fs^{-1}) but varying recoil angles to cover all
215 possible values within a hemisphere. They identified four possible final positions of ^{40}Ar. For
216 recoil vectors subparallel to the (001) plane, ^{40}Ar systematically remained in the interlayer
217 region, occupying either the initial site of the parent ^{40}K or a neighboring vacancy. For recoil
218 vectors pointing towards the T−O−T sheet, ^{40}Ar remained mainly in the interlayer region
219 (79.5 %) but also penetrated into the T−O−T layer (20.5 %), where it ended up either in
220 the tetrahedral layer adjacent to the interlayer region (16.5 %), or in the octahedral layer
221 (1.5 %) or in the opposite tetrahedral layer (2.5 %).

222 In this work, we simulate the trajectory of the ^{40}Ar recoil in muscovite using the same
223 methodology as Szczerba et al. (2015). Since the penetration of ^{40}Ar into the T−O−T layer
224 induces deformations in the crystal structure (Szczerba et al., 2015), and ClayFF being a
225 non-reactive force field designed to model undeformed structures (Cygan et al., 2004), we
226 investigated recoil trajectories parallel to the interlayer region only. We consider that ^{40}Ar
227 penetrates into the muscovite T−O−T layer in the same proportions as in illite, due to

8

the similarity of their structures. We define the recoil angle ϕ as the angle between the crystallographic direction a and the recoil vector. The simulations were carried out for recoil angles from $0°$ to $360°$ with a step of $20°$. In order to simulate a system under geological conditions, we equilibrated first the system in the NPT ensemble, at a temperature of 500 °C and a pressure of 5 kbar. The recoil simulations were then carried out in the NVT ensemble, for a duration of 250 ps with a time step of 1 fs.

The simulations reveal that, in the absence of vacancies in the immediate vicinity of the parent ^{40}K initial site, when the recoil vector is oriented towards a neighboring potassium atom (i.e. for $\phi = 0°$, $60°$, $120°$, $180°$ and $240°$) the radiogenic ^{40}Ar bounces back from that neighboring K^+ and returns to its initial interlayer position. For the other recoil angles, ^{40}Ar is first propelled into an interstitial position where it remains for about 50 ps, before either returning in its initial position or replacing a neighboring K^+ which is in turn pushed into the ^{40}Ar initial site. Along with Szczerba et al. (2015), this is the first theoretical verification that radiogenic ^{40}Ar initially resides predominantly close to its production site in K−bearing phyllosilicates (Dong et al., 1995), and not many unit cells away as sometimes suggested.

The variation of the total energy of the system when the radiogenic ^{40}Ar is propelled into the interstitial site was computed relative to the mean energy of the system when ^{40}Ar resides in a regular interlayer site. The simulations reveal that when ^{40}Ar is in the interstitial site, i.e., during the first 50 ps, the system has a mean total energy of about 100 kcal.mol^{-1} higher than when ^{40}Ar occupies a regular interlayer site (Fig. 2). This energy increase is due to the distortion that ^{40}Ar causes to the muscovite structure because of its large size. Simulation snapshots (not shown) reveal that when ^{40}Ar is located in the interstitial position, it repeals its neighboring basal oxygens, increasing locally the interlayer spacing by ca. 15 %. This is a highly unfavourable configuration energetically, precluding protracted ^{40}Ar residence in the interstitial site and making unlikely a reincorporation of ^{40}Ar into the interstitial sites once it has lost its initial recoil velocity. This rules out interstitial mechanism as a viable mechanism for ^{40}Ar diffusion in muscovite on geologic timescales.

5. Pathways and ^{40}Ar diffusion barriers in muscovite

The foregoing simulations suggest that the easiest way for ^{40}Ar to move within the muscovite structure without causing major distortions is by jumping into neighboring interlayer vacancies. Vacancies are always present in minerals. They form at high temperature to reduce the Gibbs free energy of the crystal (Mehrer, 2007). Beside those intrinsic vacancies, additional vacancies can be introduced in the mica interlayer region via the pyrophyllitic substitution $Si + \square \rightarrow {}^{IV}Al + K$ (Tardy and Fritz, 1981; Aagaard and Helgeson, 1983; Helgeson and Aagaard, 1985; Wang and Banno, 1987; Baldelli et al., 1989; Wunder and Melzer, 2002). Their abundance estimated from the commonly measured stochiometric deficit of interlayers cations (up to ca. 10 %) suggests that they can be involved in the motion of interlayer atoms. Therefore, we performed MD simulations in which we initially positioned ^{40}Ar in an interlayer K^+ site and added interlayer vacancies in its vicinity. Simulations were performed in the NPT ensemble at temperatures of 650 to 750 °C and $P = 5$ kbar, for time durations up to 25 ns. No migration could be observed; neither ^{40}Ar nor K^+ atoms jumped into the vacancies. This immobility suggests high migration energy barriers, making diffusion through a vacancy mechanism an infrequent event, unobservable on the timescales of classical MD.

To overcome the timescale limitation, we studied ^{40}Ar diffusion using TST. This requires the migration paths and the migration energies of diffusing atom to be determined first, unlike classical MD simulations which only require initial positions and velocities of atoms. The ^{40}Ar migration energies from its interlayer sites to neighboring vacancies were computed using the NEB method. Since the value of the migration energy in Eqs. (6) and (8) corresponds to the migration barrier of a system at the absolute zero, we first equilibrated the system via NPT simulations at $P = 0$ kbar and $T = -273.1$ °C (i.e., 0.5 K since there is no dynamics at 0 K). The migration of ^{40}Ar in the muscovite interlayer region depends on the presence of a vacancy in its immediate vicinity. Since vacancies can initially form far from the ^{40}Ar site, a motion of potassium atoms along the interlayer region is required for a vacancy to end next to ^{40}Ar so the K^+ migration barriers must be also determined. Furthermore, because vacancies move essentially either individually or by pairs (vacancy clusters involving more than two vacancies being thermodynamically less stable; Mehrer, 2007), we considered the migration barriers for these two configurations, i.e., the migration energies of ^{40}Ar and K^+

10

285 from their sites towards a simple vacancy (monovacancy mechanism, labelled "□"; Fig. 3a),

286 or towards a vacancy adjacent to another vacancy (divacancy mechanism, labelled "□□";

287 Fig. 3b). As the environment around each interlayer site is variable, in particular because

288 of the irregular distribution of Al in the tetrahedral layers, the statistical (probabilistic)

289 calculations must take into account the configuration of atoms in the vicinity of ^{40}Ar and K^+.

290 We positioned thus the ^{40}Ar and K^+ in all the interlayer sites of the model and computed

291 the migrations energies towards all possible neighboring sites. The charge deficit induced

292 by the incorporation of ^{40}Ar and vacancies into the interlayer region was compensated by

293 substituting Al atoms for Si in tetrahedral sites far from the ^{40}Ar migration path (some unit

294 cells away). Our results show that, in the case of the divacancy mechanism, the migration

295 barriers related to the "black" jumps (Fig. 3b) are identical to the energy barriers associated

296 with the monovacancy mechanism. Therefore, we report below 216 migration energies for the

297 monovacancy mechanism (all possible combinations), and 432 for the divacancy mechanism

298 (corresponding only to the "blue" jumps).

299 5.1. ^{40}Ar migration barriers

300 The energy barriers associated with the interlayer migration of ^{40}Ar towards neighboring

301 vacancies display wide distributions (Fig. 4a, b). The migration barriers associated with the

302 monovacancy mechanism yield a mean value of 71 ± 5 kcal.mol^{-1} (1σ), while those related to

303 the divacancy mechanism show a slightly lower but statistically indistinguishable mean value

304 of 69 ± 6 kcal.mol^{-1} (1σ). These values are similar to the energy barrier of 69 kcal.mol^{-1}

305 computed using DFT for the migration of Ar in lizardite (Wang et al., 2020), which consists of

306 a stacking of tetrahedral and octahedral layers like muscovite (Mellini, 1982). The similarity

307 between the migration barriers related to both mechanisms is illustrated by the variation

308 of the ^{40}Ar potential energy along its migration path between two neighboring stable sites

309 (corresponding to images "1" and "8"; Fig. 4c). In this example, the energy barrier related

310 to the migration of ^{40}Ar towards a single vacancy is 65 kcal.mol^{-1} while that associated with

311 the jump of ^{40}Ar into a pair of vacancies is 61 kcal.mol^{-1}. In both cases, the forward and

312 backward migration barriers are similar, and this has been observed for all computed paths.

313 The minimum energy paths followed by ^{40}Ar during these jumps (Fig. 4d) reveal that when

314 jumping into a single vacancy, ^{40}Ar follows an almost rectilinear trajectory, passing directly

11

315 below the basal oxygens crossed along the path. When it migrates into a pair of vacancies,

316 ^{40}Ar follows a similar trajectory but avoids the basal oxygens, passing quite closer to the

317 vacancy not involved in the migration path. The slight difference in trajectories shows that

318 the difference in magnitude between the respective migration barriers is directly related to

319 the presence or not of a K^+ around the pathway.

320 The migration barriers are anticorrelated to the total electrostatic energies calculated for

321 each Ar-vacancy configuration in the muscovite model (Fig. 4e). Ruiz Pestana et al. (2017)

322 also report such anticorrelation between the potassium migration energies and the cohesive

323 energies of K^+ at stable sites in illite. These observations suggest that the observed variability

324 in the magnitude of the energy barriers in our model is related to the nonuniform distribution

325 of electrostatic charges around the migration paths, which results from the irregular distri-

326 bution of Al atoms in the tetrahedral layers. The highest migration barriers are related to

327 paths with less tetrahedral Al around, in contrast to the lowest energies obtained for those

328 surrounded by more tetrahedral Al. In addition to the irregular distribution of tetrahedral

329 Al atoms, variations in the magnitude of migrations barriers also depend to some extent on

330 the relative position of the octahedral vacancies with respect to the migration path. In $2M_1$

331 muscovite, the projection of octahedral cations and interlayer atoms (K^+) on the (001) plane

332 shows that the octahedral vacancies are located directly above the migration paths forming

333 angles of $\pm$ 60 $^\circ$ and $\pm$ 120 $^\circ$ with the a axis. We observe that for migration paths with

334 the same number of surrounding tetrahedral Al, migration energies are systematically higher

335 for paths parallel to the a axis. These observations suggest a non-negligible effect of the

336 mica structure on the intrinsic diffusion of ^{40}Ar within the interlayer region, as suggested by

337 previous observations and empirical predictions (Scaillet et al., 1992; Dahl, 1996).

5.2. K^+ migration barriers

339 As with ^{40}Ar, the K^+ migration barriers define wide distributions (Fig. 5a, b). Migrations

340 energies towards monovacancies show a mean value of 79 $\pm$ 9 kcal.mol^{-1} (1σ). Using DFT

341 simulations, Yu et al. (2016) computed energy barriers associated with the migration of

342 K^+ towards a single vacancy in muscovite, for atomic models differing in their number of

343 tetrahedral Al surrounding the interlayer region where the migrating potassium is located.

344 They report energy barriers of (i) 82 kcal.mol^{-1} for the Al$-$Al model which contains Al

12

345 atoms in the two tetrahedral layers adjacent to the interlayer region; (ii) 146 kcal.mol^{-1} for

346 the Al−Si model in which Al atoms are present only in one of the tetrahedral layers, and

347 (iii) 227 kcal.mol^{-1} for the Si−Si model with tetrahedral layer adjacent to the considered

348 interlayer layer region fully occupied by Si atoms. Noteworthy, the energy barrier reported

349 for their Al−Al model, which is equivalent to ours, is within the range of values computed in

350 our study with ClayFF. Ruiz Pestana et al. (2017) report a distribution of K$^+$ energy barriers

351 in illite computed via ClayFF and DFT. They get mean values of 54 ± 12 kcal.mol^{-1} for

352 ClayFF energy barriers and 75 ± 8 kcal.mol^{-1} for those computed using DFT. They conclude

353 that ClayFF underestimates energy barriers due to the non-bonded nature of the force field

354 which makes structures excessively deformable. However, this apparent discordance between

355 ClayFF and DFT is probably related to the fact that Ruiz Pestana et al. (2017) performed

356 their ClayFF simulations without prior equilibration of their illite structure. In our study,

357 the K$^+$ energy barriers computed using ClayFF after prior equilibration of the muscovite

358 structure are in the range of their DFT-computed barriers.

359   The K$^+$ energy barriers associated with the divacancy mechanism yield a mean value of 66

360 ± 10 kcal.mol^{-1} (1σ). This value is significantly lower than the mean energy barrier related

361 to the migration of K$^+$ into a single vacancy. This pronounced difference is illustrated by the

362 variation of the potential energy along the K$^+$ migration path between two adjacent stable

363 sites (Fig. 5c). In this example, the K$^+$ energy barrier associated with the monovacancy

364 mechanism is 70 kcal.mol^{-1} and the K$^+$ energy barrier related to the divacancy mechanism

365 55 kcal.mol^{-1}. The minimum energy paths followed by K$^+$ during these migrations show

366 that, in both cases, the potassium atom follows a curvilinear trajectory avoiding the basal

367 oxygen atoms along the path (Fig. 5d). However, in the case of the divacancy mechanism,

368 potassium passes further away from the oxygen atoms than in the monovacancy mechanism.

369 This suggests that the decrease in the migration energy is due to the ability of K$^+$ ions to

370 minimize interactions with the oxygen atoms lying on their path. Moreover, while ^{40}Ar is

371 at the same energy level in two neighboring vacancies, potassium shows an energy difference

372 between the two sites (Fig. 5c). This is because potassium (charged) is more sensitive to the

373 local charge distribution than ^{40}Ar (neutral). Despite these structural-charge differences, the

374 K$^+$ and ^{40}Ar energy barriers are positively correlated (Fig. 5e), suggesting a similar influence

13

375 of the local environment on the migration energy landscape.

376 6. ^{40}Ar diffusion coefficients

377 In this section, we calculate the ^{40}Ar diffusion coefficients in muscovite for both the
378 monovacancy and the divacancy mechanisms by TST (Eq. (8)). Since the investigated
379 migrations occur along the interlayer region, we perform calculations for 2D diffusion in a
380 hexagonal lattice. As given above, Eq. (8) allows the analytical derivation of the diffusion
381 coefficient for a pristine and homogenous crystal, i.e., a crystal in which the migration barrier
382 is the same for all equivalent jumps. In our case, because of the irregular distribution of Al
383 atoms in the tetrahedral layers, the energy barriers of interlayer atoms vary from one direction
384 to another, and from one interlayer site to another. To take into account the spatial variation
385 of the migration barrier, we consider for each diffusing atom an overall effective migration
386 energy, E_{eff}, defined as:

$$\exp\left(\frac{E_{\mathrm{eff}}}{RT}\right) = \sum_{i=1}^{n} \frac{1}{n} \exp\left(\frac{E_i}{RT}\right) \tag{10}$$

388 where E_i is the effective energy barrier required for an atom to leave an interlayer site i and
389 n is the total number of stable sites in the interlayer region. The effective energy barrier for
390 each site (E_i) is derived from:

$$\exp\left(\frac{-E_i}{RT}\right) = \sum_{j=1}^{m} \frac{1}{m} \exp\left(\frac{-E_{ij}}{RT}\right) \tag{11}$$

392 in which E_{ij} is the migration energy for leaving the interlayer site i in the direction j, and
393 m is the number of all possible directions ($m = 6$ in a hexagonal lattice).

394 Eqs (10) and (11) are justified by making an analogy with an electric circuit. When
395 different paths from a given site are possible, the conductances of the paths add up. As the
396 conductance is proportional to the Boltzmann factor, this leads to Eq. (11). A consequence
397 is that the path having the lowest migration energy dominates. When considering a set of
398 sites, they are travelled in sequence so that the resistances add up as expressed by Eq. (10).
399 In particular a site having a high migration energy will slow down the entire diffusion process,
400 this is the trapping effect. Using the energy barriers calculated in section 5, we obtain effective
401 ^{40}Ar migration energy barriers $E_{\mathrm{eff}}^{\mathrm{Ar}\square} = 69$ kcal.mol^{-1} and $E_{\mathrm{eff}}^{\mathrm{Ar}\square\square} = 65$ kcal.mol^{-1} for the

14

402 monovacancy and the divacancy mechanism, respectively. For K^+ (or vacancy) migration,

403 the calculated effective barriers are $E_{\text{eff}}^{K\square} = 75$ kcal.mol^{-1} (monovacancy mechanism) and

404 $E_{\text{eff}}^{K\square\square} = 58$ kcal.mol^{-1} (divacancy mechanism).

405 *6.1. Monovacancy mechanism*

406 *6.1.1. Diffusion of monovacancies in a hexagonal lattice of K^+*

407 The diffusion of ^{40}Ar via the monovacancy mechanism requires the presence of a vacancy

408 in one of its neighboring sites. As long as no vacancies are available, ^{40}Ar cannot move,

409 requiring first to study the diffusivity of the vacancies in the interlayer region. When a

410 vacancy is present in the interlayer region, it is filled by the jump of a neighboring K^+ which,

411 in turn, releases a vacancy in its initial site (Fig. 3a). The displacement vectors have as

412 components:

$$413 \quad \overrightarrow{V_0} = \begin{pmatrix} \frac{1}{2}a \\ \frac{\sqrt{3}}{2}a \end{pmatrix} \; \overrightarrow{V_1} = \begin{pmatrix} -\frac{1}{2}a \\ \frac{\sqrt{3}}{2}a \end{pmatrix} \; \overrightarrow{V_2} = \begin{pmatrix} -a \\ 0 \end{pmatrix} \; \overrightarrow{V_3} = \begin{pmatrix} -\frac{1}{2}a \\ -\frac{\sqrt{3}}{2}a \end{pmatrix} \; \overrightarrow{V_4} = \begin{pmatrix} \frac{1}{2}a \\ -\frac{\sqrt{3}}{2}a \end{pmatrix} \; \overrightarrow{V_5} = \begin{pmatrix} a \\ 0 \end{pmatrix} \quad (12)$$

414 and the variance of the displacement of the vacancy is:

$$\Delta x^2 = \Delta y^2 = \frac{a^2}{2} \tag{13}$$

416 We denote by $\gamma_{K\square}$ the frequency of the jump of one of the neighbouring K^+ towards a

417 monovacancy (noted $K^+ \leftrightarrows \square$), ν the attempt frequency, and $E_{\text{eff}}^{K\square}$ the migration barrier of

418 K^+. According to TST, the jump frequency is given by:

$$\gamma_{K\square} = \nu \exp\left(- \frac{E_{\text{eff}}^{K\square}}{RT} \right) \tag{14}$$

420 The timelife of the vacancy (i.e., the average time for a successful displacement) is:

$$\Delta t_K = \frac{1}{6\gamma_{K\square}} \tag{15}$$

422 and the 2D diffusion coefficient of the vacancy is:

$$D_\square = \frac{\Delta x^2 + \Delta y^2}{4\Delta t_K} = \frac{3}{2}a^2\nu \exp\left(- \frac{E_{\text{eff}}^{K\square}}{RT} \right) \tag{16}$$

424 where a is the distance between two neighboring interlayer sites ($a = 5.2$ Å). At $T = 700$ °C,

425 the diffusion coefficient of a single vacancy is $D_\square = 2.88 \times 10^{-19}$ cm^2.s^{-1}.

15

6.1.2. ^{40}Ar diffusion in a monovacancy flux

Each time a vacancy gets next to a ^{40}Ar atom it is surrounded by five K$^+$ ions. Interchange between the ^{40}Ar and vacancy positions (noted ^{40}Ar $\leftrightarrows \square$) occurs due to thermal agitation and the lower barrier potential of ^{40}Ar $\leftrightarrows \square$ relative to K$^+$ $\leftrightarrows \square$. The average duration of these Ar-vacancy oscillations is therefore:

$$\Delta t_{\text{osc}} = \frac{1}{5\gamma_{K_\square}} \tag{17}$$

During this time, many oscillations will have occurred with equal probability 0.5 of ending up either in the initial configuration (no exchange) or in effective migration of ^{40}Ar into the vacancy. The oscillations stop when one of the five K$^+$ neighbors jumps into the vacancy. For three of these K$^+$, a successful jump will remove the vacancy away from ^{40}Ar, stopping the ^{40}Ar $\leftrightarrows \square$ oscillations. For the other two, the vacancy stays in the vicinity of ^{40}Ar and the oscillations can resume among the newly created Ar-vacancy pair.

Summing up, when a vacancy gets close to ^{40}Ar, after an average time Δt_{osc}, four different configurations are possible:

- The vacancy has gone away leaving ^{40}Ar in its initial position with a probability of 3/10.

- The vacancy has moved into one of the two neighboring positions of ^{40}Ar with a probability of 2/10. Oscillations resume among the newly-created ^{40}Ar-vacancy pair.

- The ^{40}Ar $\leftrightarrows \square$ interchange is successful and the vacancy moves further away by more than one lattice position with probability of 3/10.

- The ^{40}Ar $\leftrightarrows \square$ interchange has occurred but leaving the vacancy next to ^{40}Ar with probability of 2/10. Oscillations resume again among the new Ar-vacancy pair.

The average number of jumps $\langle n_s \rangle$ needed to move the vacancy away from ^{40}Ar can be calculated by combining the respective probabilities:

$$\langle n_s \rangle = \frac{3}{5} \sum_{n=1}^{\infty} n \left(\frac{2}{5}\right)^{n-1} = \frac{5}{3} \frac{1}{(1-2/5)^2} = \frac{5}{3} \tag{18}$$

According to Eq. (18), the average residence time of the vacancy in the vicinity of ^{40}Ar (the timelife of this configuration) is:

$$\Delta t_o = \frac{5}{3} \Delta t_{\text{osc}} = \frac{1}{3\gamma_{K_\square}} \tag{19}$$

16

453 During this time interval, several trains of oscillations will have occured. The calculation
454 of the variance of the mean displacement of ^{40}Ar is complicated by the fact the successive
455 displacements are correlated. However, KMC simulations show that the positional variance
456 of the displacement of $\square$ along either $\overrightarrow{x}$ or $\overrightarrow{y}$ is completely defined by the number of jumps
457 n_s of the vacancy remaining in the neighborhood:

$$\langle \Delta x^2 \rangle = \langle \Delta y^2 \rangle = \frac{n_s + 1}{8} a^2 \tag{20}$$

459 By summing over the n_s probabilities, we obtain the average variance resulting in the nearest-
460 neighbor vacancy configuration:

$$\langle \Delta x^2 \rangle = \langle \Delta y^2 \rangle = \frac{a^2}{3} \tag{21}$$

462 Note that, despite its higher energy barrier, the variance is stochastically dominated by the
463 bulk motion of K$^+$ via the K$^+ \leftrightarrows \square$ interchange (vacancy diffusion), not the mobility of ^{40}Ar
464 with respect to the vacancy. The vibrational motion of ^{40}Ar just ensures that it will take
465 (with probability 0.5) a quantum step away from its initial position when the vacancy passes
466 close by. Note also that this is the variance induced by the proximity of a vacancy. Most of
467 the time, no vacancy hangs around ^{40}Ar which cannot move then (the time goes on with the
468 variance remaining unchanged).

469 We now inquire into the bulk vacancy flux that governs the overall mobility of ^{40}Ar
470 through the muscovite interlayer. Consider a portion of lattice containing N regular interlayer
471 sites with a single ^{40}Ar atom and a density of vacancies ρ. The number of neighboring
472 sites around a vacancy is six and the number of vacancies $N\rho$. At each vacancy jump, the
473 probability of starting from either a normal "bulk" position or next to ^{40}Ar is proportional
474 to their respective populations. The probability of starting from a neighboring site must
475 be weighted by a factor of 5/6 because only five directions allow it to be reached, instead
476 of six for a normal site. This quantitative reduction has been tested by KMC simulation
477 (Appendix A). Finally, during a vacancy jump the probability of starting from a bulk site is
478 $P_b = (N - 6)/N$ while that of jumping from the vicinity of ^{40}Ar is $P_v = 6/N(5/6) = 5/N$.

479 Consider now a trajectory of m jumps of the $N\rho$ vacancies. Among these m jumps
480 mP_b will start from a bulk site whose lifetime is $t_b = 1/(6\gamma_{K_\square})$ and mP_v will come from

17

481 neighboring sites with lifetime $t_v = 1/(5\gamma_{K_\square})$. The total duration of these trajectories of m

482 jumps is therefore:

$$t = m\left(1 - \frac{6}{N}\right)\frac{1}{6\gamma_{K_\square}} + m\frac{5}{N}\frac{1}{5\gamma_{K_\square}} = \frac{m}{6\gamma_{K_\square}} \tag{22}$$

484 The average number of vacancy jumps ending next to ^{40}Ar is:

$$m_v = m\frac{5}{N}N\rho = 5\rho\,m \tag{23}$$

486 We have seen that in the direct-neighbor configuration (Fig. 3a), on average 5/3 jumps move

487 the vacancy away from ^{40}Ar (Eq. (18)). The number of such moves in a bulk vacancy flux

488 is:

$$m'_v = 3\rho\,m \tag{24}$$

490 According to Eq. (21), each of these moves has variance $a^2/3$ so that on average:

$$\langle\Delta x^2\rangle = \langle\Delta y^2\rangle = \rho a^2\,m = 6\rho\gamma_{K_\square}a^2\,t \tag{25}$$

492 The diffusion coefficient for ^{40}Ar is thus:

$$D_{\mathrm{Ar}_\square} = \frac{\langle x^2\rangle + \langle y^2\rangle}{4\,t} = 3\,a^2\,\gamma_{K_\square}\,\rho = 3\,a^2\,\nu\,\rho\,\exp\left(-\frac{E_{\mathrm{eff}}^{\mathrm{K}_\square}}{RT}\right) \tag{26}$$

494 The temperature dependence of this diffusion mechanism is reported in the Arrhenius

495 diagram (Fig. 6). For example, at $T = 700\,^\circ$C and $\rho = 0.1$, the diffusion coefficient is $D_{\mathrm{Ar}_\square} =$

496 5.76×10^{-20} cm^2.s^{-1}. The diffusion parameters associated with the monovacancy mechanism

497 are $E = 75$ kcal.mol^{-1} and $D_0 = 4 \times 10^{-3}$ cm^2.s^{-1}.

498 *6.2. Divacancy mechanism*

499 *6.2.1. Diffusion of divacancies in a hexagonal lattice of K^+*

500 In the case of a divacancy mechanism, K$^+$ atoms are adjacent either to only one vacancy

501 or both (Fig. 3b). In the latter configuration, the jumps (blue arrows) have a lower effective

502 energy barrier (58 kcal.mol^{-1}) and therefore a higher probability of occurrence than those of

503 the first configuration (in black), whose migration barriers are identical to those associated

504 with the monovacancy mechanism (75 kcal.mol^{-1}). When one of these "blue" migrations

505 occurs, a K$^+$ atom fills one vacancy and a new vacancy is created in its initial position.

506 This new vacancy lies in one of the sites neighboring the unoccupied vacancy of the initial

18

pair, and both form a new vacancy pair. Therefore, one can expect a correlated mobility of divacancies along the interlayer region.

The two pertinent quantities to calculate here are the diffusion coefficient of the divacancy and its lifetime. The divacancy is characterized by its position (barycenter of the vacancy pair), the direction passing through the vacancy pair, and the angle made by the direction with the x-axis which can be $0°$ (Fig. 3b) or $\pm 60°$. Each atom jump filling a vacancy produces a virtual displacement and the apparent rotation of the divacancy direction. Let us calculate the average variance of such a displacement.

When the starting angle is $0°$ the jumps $\overrightarrow{\delta_0}$, $\overrightarrow{\delta_1}$, $\overrightarrow{\delta_2}$, $\overrightarrow{\delta_3}$ produce respectively the angles $60°$, $60°$, $-60°$, $-60°$, and the divacancy displacement vectors:

$$\overrightarrow{V_0} = \begin{pmatrix} \frac{1}{4}a \\ \frac{\sqrt{3}}{4}a \end{pmatrix} \qquad \overrightarrow{V_1} = \begin{pmatrix} -\frac{1}{4}a \\ -\frac{\sqrt{3}}{4}a \end{pmatrix} \qquad \overrightarrow{V_2} = \begin{pmatrix} \frac{1}{4}a \\ -\frac{\sqrt{3}}{4}a \end{pmatrix} \qquad \overrightarrow{V_3} = \begin{pmatrix} -\frac{1}{4}a \\ \frac{\sqrt{3}}{4}a \end{pmatrix} \tag{27}$$

By symmetry, these jumps are equiprobable.

For a starting angle of $60°$, the divacancy displacement vectors $\overrightarrow{V_i}$ are just rotated by this angle :

$$\overrightarrow{V_i}' = \begin{pmatrix} \frac{1}{2} & -\frac{\sqrt{3}}{2} \\ \frac{\sqrt{3}}{2} & \frac{1}{2} \end{pmatrix} \overrightarrow{V_i} \tag{28}$$

and:

$$\overrightarrow{V_0}' = \begin{pmatrix} -\frac{1}{4}a \\ \frac{\sqrt{3}}{4}a \end{pmatrix} \qquad \overrightarrow{V_1}' = \begin{pmatrix} \frac{1}{4}a \\ -\frac{\sqrt{3}}{4}a \end{pmatrix} \qquad \overrightarrow{V_2}' = \begin{pmatrix} \frac{1}{2}a \\ 0 \end{pmatrix} \qquad \overrightarrow{V_3}' = \begin{pmatrix} -\frac{1}{2}a \\ 0 \end{pmatrix} \tag{29}$$

For the $-60°$ configuration, the corresponding rotation is:

$$\overrightarrow{V_0}'' = \begin{pmatrix} \frac{1}{2}a \\ 0 \end{pmatrix} \qquad \overrightarrow{V_1}'' = \begin{pmatrix} -\frac{1}{2}a \\ 0 \end{pmatrix} \qquad \overrightarrow{V_2}'' = \begin{pmatrix} -\frac{1}{4}a \\ -\frac{\sqrt{3}}{4}a \end{pmatrix} \qquad \overrightarrow{V_3}'' = \begin{pmatrix} \frac{1}{4}a \\ \frac{\sqrt{3}}{4}a \end{pmatrix} \tag{30}$$

Whatever the starting configuration, it can be shown that $\langle x \rangle = \langle x \rangle = 0$. For a given trajectory, the orientations are equiprobable. For all jumps keeping the vacancy pair connected the displacements $\overrightarrow{V_i}, \overrightarrow{V_i}'$ and $\overrightarrow{V_i}''$ occur with equal probability of $1/12$. One may verify that $\langle x \cdot y \rangle = 0$, indicating that the displacements along either x or y are uncorrelated which is a consequence of hexagonal symmetry. In terms of variance of displacements we have:

$$\langle x^2 \rangle = \langle y^2 \rangle = \frac{1}{8}a^2 \tag{31}$$

19

532 due again to the symmetry in x and y.

533 Denote by $\gamma_{K_\square}$ the jump frequency corresponding to a "black" migration and $\gamma_{K_{\square\square}}$ for

534 the "blue" migration (Fig. 3b). The residence time of the divacancy at any given position is:

$$t_r = \frac{1}{4\gamma_{K_{\square\square}} + 6\gamma_{K_\square}} \tag{32}$$

536 The average migration time after m jumps is:

$$\langle t \rangle = m\, t_r = \frac{m}{4\gamma_{K_{\square\square}} + 6\gamma_{K_\square}} \tag{33}$$

538 and the variance of the displacement:

$$\langle x^2 \rangle = \langle y^2 \rangle = m\frac{a^2}{8} \tag{34}$$

540 From these, we deduce the divacancy diffusion coefficient:

$$D_{\square\square} = \frac{1}{4}a^2\left(\gamma_{K_{\square\square}} + \frac{3}{2}\gamma_{K_\square}\right)$$

542

$$D_{\square\square} = \frac{1}{4}a^2\nu\exp\left(-\frac{E_{\text{eff}}^{K_{\square\square}}}{RT}\right)\left[1 + \frac{3}{2}\exp\left(\frac{E_{\text{eff}}^{K_{\square\square}} - E_{\text{eff}}^{K_\square}}{RT}\right)\right] \tag{35}$$

544 where $E_{\text{eff}}^{K_{\square\square}}$ is the K^+ migration barrier towards a divacancy. The second exponential in

545 parentheses (rightmost term) is much smaller than unity and the diffusion coefficient reduces

546 to:

$$D_{\square\square} = \frac{1}{4}a^2\nu\exp\left(-\frac{E_{\text{eff}}^{K_{\square\square}}}{RT}\right) \tag{36}$$

548 At $T = 700$ °C, the diffusion coefficient associated with the divacancy migration is $D_{\square\square} =$

549 3.89×10^{-16} cm^2.s^{-1}, three orders of magnitude faster than the monovacancy mechanism.

550 *6.2.2. ^{40}Ar diffusion in a divacancy flux*

551 When a divacancy lies in the vicinity of ^{40}Ar, the latter can be adjacent to either one

552 or both vacancies and the probability that one is filled by ^{40}Ar depends on the specific

553 nearest-neighbor configuration. Denote by $E_{\text{eff}}^{Ar\square}$ the ^{40}Ar energy barrier faced by the "black"

554 transitions and by $E_{\text{eff}}^{Ar\square\square}$ that associated with "blue" migrations. When the ^{40}Ar is adjacent

555 to only one of the two vacancies (Fig. 3b) the probability of jump before a move of the

20

divacancy is:

$$P_{\text{Ar}_\square} = \frac{\exp\left(-\dfrac{E_{\text{eff}}^{\text{Ar}_\square}}{RT}\right)}{\exp\left(-\dfrac{E_{\text{eff}}^{\text{Ar}_\square}}{RT}\right) + 5\exp\left(-\dfrac{E_{\text{eff}}^{\text{K}_\square}}{RT}\right) + 2\exp\left(-\dfrac{E_{\text{eff}}^{\text{K}_{\square\square}}}{RT}\right)}$$

$$= \frac{\exp\left(-\dfrac{E_{\text{eff}}^{\text{Ar}_\square} - E_{\text{eff}}^{\text{K}_{\square\square}}}{RT}\right)}{\exp\left(-\dfrac{E_{\text{eff}}^{\text{Ar}_\square} - E_{\text{eff}}^{\text{K}_{\square\square}}}{RT}\right) + 5\exp\left(-\dfrac{E_{\text{eff}}^{\text{K}_\square} - E_{\text{eff}}^{\text{K}_{\square\square}}}{RT}\right) + 2} \tag{37}$$

The exponentials in the denominator are much smaller than one because of the difference in the energy barriers, and Eq. (37) simplifies to

$$P_{\text{Ar}_\square} = \frac{1}{2}\exp\left(-\frac{E_{\text{eff}}^{\text{Ar}_\square} - E_{\text{eff}}^{\text{K}_{\square\square}}}{RT}\right) \tag{38}$$

On the other hand, there are two positions where the ^{40}Ar is close to both vacancies (Fig. 3b) and the probability of jumping into one of them before the divacancy move is:

$$P_{\text{Ar}_{\square\square}} = \frac{\exp\left(-\dfrac{E_{\text{eff}}^{\text{Ar}_{\square\square}}}{RT}\right)}{\exp\left(-\dfrac{E_{\text{eff}}^{\text{Ar}_\square}}{RT}\right) + 6\exp\left(-\dfrac{E_{\text{eff}}^{\text{K}_\square}}{RT}\right) + \exp\left(-\dfrac{E_{\text{eff}}^{\text{K}_{\square\square}}}{RT}\right)} \tag{39}$$

As before, Eq. (39) simplifies to

$$P_{\text{Ar}_{\square\square}} = \exp\left(-\frac{E_{\text{eff}}^{\text{Ar}_{\square\square}} - E_{\text{eff}}^{\text{K}_{\square\square}}}{RT}\right) \tag{40}$$

The relative importance of the probabilities Eqs. (38) and (40) depends on the frequency of each configuration.

Denote by ρ' the density of divacancies in the interlayer region, defined as the number of divacancies divided by the number of interlayer sites in the lattice. Consider a trajectory of m jumps of the divacancies. For $6m\rho'$ positions the ^{40}Ar will be close to one only vacancy, and for $m\rho'$ it will be close to both vacancies. The above expressions can be deduced by weighing the different orientations and by observing that the double-vicinity of the ^{40}Ar can

21

574 be reached only from one side, and they have been confirmed by running dedicated KMC
575 simulations (Appendix A.).

576   In the bulk divacancy flux, the residence time of a divacancy is given by Eq. (32) in which
577 $\gamma_{K_\square}$ can be neglected. This residence time is nearly the same when a ^{40}Ar is close to only
578 one vacancy, but it doubles when it neighbors the two vacancies. Therefore the time for a
579 trajectory of m jumps is:

$$t = \frac{m}{4\gamma_{K_{\square\square}}}(1 + \rho') = \frac{m}{4\nu}(1 + \rho')\exp\left(\frac{E_{\mathrm{eff}}^{\mathrm{K}_{\square\square}}}{RT}\right) \tag{41}$$

581 For $6m\rho'$ configurations, ^{40}Ar sees only one vacancy and the jump probability is given by Eq.
582 (38). For $m\rho'$ configurations it neighbors the two vacancies and has a jump probability given
583 by Eq. (40). For any jump the variance in coordinates is given by Eq. (13). In the end, for
584 m jumps the variance is:

$$\langle x^2 \rangle = \langle y^2 \rangle = m\rho'\frac{a^2}{2}\left[3\exp\left(-\frac{E_{\mathrm{eff}}^{\mathrm{Ar}_\square} - E_{\mathrm{eff}}^{\mathrm{K}_{\square\square}}}{RT}\right) + \exp\left(-\frac{E_{\mathrm{eff}}^{\mathrm{Ar}_{\square\square}} - E_{\mathrm{eff}}^{\mathrm{K}_{\square\square}}}{RT}\right)\right] \tag{42}$$

586 From Eq. (41) and (42) we can deduce the diffusion coefficient for ^{40}Ar:

$$D_{\mathrm{Ar}_{\square\square}} = \frac{\rho'}{1 + \rho'}a^2\nu\left[3\exp\left(-\frac{E_{\mathrm{eff}}^{\mathrm{Ar}_\square}}{RT}\right) + \exp\left(-\frac{E_{\mathrm{eff}}^{\mathrm{Ar}_{\square\square}}}{RT}\right)\right] \tag{43}$$

588 in which the first term inside the brackets is small compared to the last one.

589   It remains to determine the density of divacancies ρ'. It can be expressed with the density
590 of monovacancies ρ. The divacancies are produced when two monovacancies hit each other,
591 because their coherent motion is energetically favored. On the other hand they decay when
592 one of its vacancies is filled by a neighboring K^+ (black jumps; Fig. 3). This is a dynamical
593 equilibrium reached when the rate of production equates the rate of decay.

594   Consider N regular interlayer sites. The number of monocancies is $N\rho$. At any jump
595 of a vacancy, the probability to make a collision (i.e. to reach the neighborhood of another
596 vacancy) is proportional to ρ, so that the number of produced divacancies is $kN\rho^2$, where k
597 is a number to be determined. A dedicated random walk simulation shows that $k = 2.5$. The
598 duration of each step is $1/(6\gamma_{K_\square})$ giving a production rate of $15N\rho^2\gamma_{K_\square}$. The decay rate is
599 $6N\rho'\gamma_{K_\square}$. By equating the two rates one gets $\rho' = 2.5\rho^2$.

22

600   After replacement of this value in Eq. (43) and taking into account that $\rho \ll 1$:

601
$$D_{\text{Ar}_{\square\square}} = \frac{5}{2}\rho^2 a^2 \nu \left[3\exp\left(-\frac{E_{\text{eff}}^{\text{Ar}_\square}}{RT} \right) + \exp\left(-\frac{E_{\text{eff}}^{\text{Ar}_{\square\square}}}{RT} \right) \right] \tag{44}$$

602 At $T = 700\ °\text{C}$ and for $\rho = 0.1$, the ^{40}Ar diffusion coefficient associated with the divacancy

603 mechanism is $D_{\text{Ar}_{\square\square}} = 1.16 \times 10^{-18}\ \text{cm}^2.\text{s}^{-1}$, two orders of magnitude higher than the

604 diffusivity of the monovacancy mechanism. The ^{40}Ar diffusion parameters deduced from the

605 Arrhenius diagram (Fig. 6) are $E = 66\ \text{kcal.mol}^{-1}$ and $D_0 = 6 \times 10^{-4}\ \text{cm}^2.\text{s}^{-1}$. A summary

606 listing of the final estimates is provided in Table 3.

607 7. Discussion

608 7.1. Comparison with previous ^{40}Ar diffusion estimates

609   As mentioned above, only a handful of studies have attempted to quantify ^{40}Ar dif-

610 fusion in muscovite (Robbins, 1972; Hames and Bowring, 1994; Kirschner et al., 1996;

611 Lister and Baldwin, 1996, 2016; Harrison et al., 2009; Forster and Lister, 2014). While

612 ^{40}Ar diffusivity estimates inferred by these studies are broadly consistent, they considerably

613 differ from the present results. Our MD and TST estimates are up to five orders of magnitude

614 lower than the corresponding Arrhenian laws (Fig. 6). Note that our results are calculated

615 for muscovite at $P = 0\ \text{kbar}$. Assuming a pressure effect on diffusivity of ^{40}Ar in muscovite

616 (Harrison et al., 2009) would enhance the disparity even further.

617   Hydrothermal experiments have been suspected to overestimate ^{40}Ar diffusivity in natural

618 muscovite for quite a while now (Monié, 1990; Scaillet et al., 1990, 1992; Monié and Chopin,

619 1991; Arnaud and Kelley, 1995; Scaillet, 1996; Di Vincenzo et al., 2001, 2004, 2006; Balogh

620 and Dunkl, 2005; Hames et al., 2008; Itaya et al., 2009; Allaz et al., 2011; Beltrando et al.,

621 2013; Halama et al., 2014; Schertl and Hammerschmidt, 2016; Laurent et al., 2021). As

622 emphasized before, most of these studies relate to high-pressure (phengitic) muscovite. The

623 high retentivity (i.e., low ^{40}Ar diffusivity) of muscovite in these conditions has long been

624 traced to crystal-structural effects suspected to affect the interlayer at increasingly higher

625 pressure (Scaillet et al., 1992; Scaillet, 1998). It is also supported by the diffusion data of

626 Harrison et al. (2009) which predict lower diffusivities at high pressure. Evidence for a

627 pronounced ^{40}Ar retentivity in muscovite has been also reported in other settings as well

23

628 (e.g. Di Vincenzo et al., 2004; Hames et al., 2008; Itaya et al., 2009; Allaz et al., 2011),
629 suggesting that sluggish ^{40}Ar kinetics in natural muscovite is more the norm than currently
630 acknowledged by existing experimental data.

631 Field-based calibration of ^{40}Ar retention kinetics in muscovite is scarce and highly context-
632 specific (e.g., Wijbrans and McDougall, 1986, 1988; Blanckenburg et al., 1989; Kirschner et
633 al., 1996). So far, such efforts have been taken to indicate moderate or intermediate ^{40}Ar
634 retention properties of muscovite relative to other isotope-mineral pairs (by order of decreas-
635 ing retentivity: U/Pb−zircon > Rb/Sr−muscovite > K/Ar−amphibole > K/Ar−muscovite
636 > K/Ar−biotite ≈ K/Ar−alkali feldspar). Mounting evidence, in particular from grain-
637 scale Rb/Sr and laser-based ^{40}Ar/^{39}Ar disequilibrium data (e.g. Bröcker et al., 2013; Cliff
638 et al., 2017; Laurent et al., 2021), shows that Ar-Rb-Sr retention systematics in natu-
639 ral muscovite are actually quite similar (Glodny et al., 2002; 2008; Bosse et al., 2005;
640 Scibiorski et al., 2021), pointing to otherwise more sluggish kinetics than suggested by the
641 above trend for elements that are either ionically bonded (Rb, Sr) and/or simply too big (Ar)
642 to easily jump from a lattice position to the next. This is most clearly illustrated by peak-
643 metamorphic ^{40}Ar/^{39}Ar retention ages commonly preserved in muscovite despite deformation
644 and overprinting (Putlitz et al., 2005; Beaudoin et al., 2020, Laurent et al., 2021). This is also
645 emphasized by congruent ^{40}Ar/^{39}Ar muscovite and U/Pb titanite ages metastably preserved
646 over map-scales in excess of 450-750 km^2 in dry granulite-amphibolite crust exposed to $T \geqslant$
647 700 °C for tens of Myr (Spencer et al., 2013).

648 Using the diffusion data retrieved from our modeling ($E = 66$ kcal.mol^{-1} and $D_0 =$
649 6×10^{-4} cm^2.s^{-1}), nominal closure temperatures can be calculated via Eq. (1) for various
650 cooling rates and grain sizes. For cooling rates ranging from 1 to 100 °C.Ma^{-1} and grain
651 size varying between 0.1-1.0 mm, this returns closure temperatures in the range 560-800 °C
652 (Fig. 7). These are significantly (up to 200 °C) higher than predicted by current experimental
653 estimates (Hames and Bowring, 1994; Kirschner et al., 1996; Harrison et al., 2009) and close
654 to the upper stability limit of muscovite ($\sim$ 700 °C; Massonne and Schreyer, 1987, 1989),
655 which by the way is significantly lower in presence of quartz (Althaus et al., 1970). This
656 opens up the prospect that crystallization ages may be more likely than cooling ages in
657 natural muscovite.

24

658 However, empirical evidence also abounds to suggest that intracrystalline ^{40}Ar mobility
659 may be enhanced by other factors beyond purely diffusion-driven rates such as predicted by
660 our model. Our model calculations apply to ideal (undefective) muscovite. Natural micas
661 are far from perfect and always contain microstructural defects such as dislocations, stacking
662 faults, microcleavages, etc., which can develop during crystal growth, or more commonly, in
663 response to deformation (e.g. Bell and Wilson, 1977, 1981; Amouric, 1987; Kronenberg et
664 al., 1990; Shea and Kronenberg, 1992; Dunlap, 1997; Beaudoin et al., 2020). Such extended
665 microstructural defects act as high diffusivity pathways that can considerably enhance the
666 mobility of diffusing atoms (Lee, 1995). Sizeable extents of ^{40}Ar loss have been documented in
667 naturally and experimentally deformed muscovite in connection with microstructural defects
668 (Kramar et al., 2001, 2003; Mulch et al., 2002; Cosca et al., 2011). Ascribing the observed
669 losses in such cases to diffusion only is bound to overestimate ^{40}Ar diffusion rates, but to a
670 largely unknown extent if the crystal-defective structure of the mica is not properly quantified
671 (Kramar et al., 2001, 2003). A case in point are the diffusion rates empirically derived from
672 the muscovites studied by Kirschner et al. (1996). These crystallized during deformation by
673 thrusting and most likely contain microstructural defects as well.

674 The same caveat applies to diffusion experiments performed under hydrothermal condi-
675 tions (Dunlap, 1997). To optimize the fractional loss of their starting material, Harrison et
676 al. (2009) used fine-grained muscovite fractions ($< 100\ \mu$m across) obtained by mechanical
677 grinding of larger grains. Such grinding is likely to have produced extended intracrystalline
678 defects in their samples, a problem already raised by Dunlap (1997) for the early thermal-
679 hydrothermal experiments conducted by Robbins (1972). While these defects may have little
680 effect on the effective loss of ^{40}Ar in vacuum (< 0.5 %; Dunlap and Kronenberg, 2001), their
681 impact under hydrothermal conditions may be vastly underestimated because of the longer
682 duration of these experiments. Incidentally, Harrison et al. (2009) used a multi-domain
683 diffusion model in an attempt to fit their hydrothermal-loss data to complex *in vacuo* gen-
684 erated ^{40}Ar/^{39}Ar spectrum patterns. Such a non-ideal behavior may to some extent reflect
685 the complex defective structure artificially induced during sample preparation.

686 An additional complication is the presence of reactive fluids, both in Nature and exper-
687 iments. When out of equilibrium with the solid phase, fluid-phase dissolution-precipitation

25

688 may lead to partial destabilization depending on fluid-solid equilibria, crystal boundary struc-
689 ture and width, and exchange duration (Cole and Chakraborty, 2001; Putnis, 2009). Fluid-
690 phase dissolution kinetics are much faster than solid-state intracrystalline diffusion (Scaillet,
691 1998; Putnis, 2009), potentially enhancing ^{40}Ar loss well beyond lattice diffusion rates in
692 hydrothermal experiments. Harrison et al. (2009) report a fractional loss 10 % higher for
693 a hydrothermal run compared to the same $P-T$ run under dry conditions. Although the
694 authors infer that a fluid phase is a necessary reservoir for ^{40}Ar to be diffusively lost from
695 muscovite during the experiments, the difference may also reflect ^{40}Ar diffusion enhanced
696 in the presence of water. Harrison et al. (2009) also report an Al enrichment of their run
697 products compared to the starting material. As discussed by Villa (2021), this may hint
698 at dissolution−precipitation transformations during the runs, potentially compromising (i.e.,
699 overestimating) the diffusion rates derived from the observed losses. Evidence of recrystal-
700 lization of micas during hydrothermal experiments is also reported by Hess et al. (1987) and
701 Villa and Puxeddu (1994).

702   Although not dealing with ^{40}Ar diffusion in muscovite proper, studies of Sr diffusion in
703 biotite (Hammouda and Cherniak, 2000) have revealed four orders magnitude difference in
704 diffusion rates between hydrothermally treated biotite (faster-diffusing) and dry F-phlogopite
705 (slower-diffusing). These authors rule out F-substitutional effects in favor of the weaken-
706 ing effect of water on the mica structure to explain this behavior, possibly enhanced by
707 dissolution−recrystallization processes during the hydrothermal treatment. Water molecules
708 can also act as source of H$^+$, which weaken Si−O and Al−O bonds and consequently en-
709 hance the diffusion of oxygen in minerals such as quartz (Elphick and Graham, 1988), al-
710 kali feldspar (Farver and Yund, 1990) and micas (Fortier and Giletti, 1991). Hydrolysis of
711 K−O bonds in muscovite, similar to that of Si−O and Al−O in other common silicates,
712 could lower the ^{40}Ar migration barrier, thereby accelerating its diffusion. All these mecha-
713 nisms suggests that ^{40}Ar diffusivity measured under hydrothermal conditions provides only
714 an upper limit to actual ^{40}Ar transport rates across the mica lattice.

715 *7.2. Applicability to natural systems and implications for $^{40}Ar/^{39}Ar$ thermochronology*

716   All the above processes work the same in Nature, but with even more free thermodynamic
717 variables (e.g., multiphase equilibria, transient fluids) and much longer durations than in hy-

26

718 drothermal diffusion cells. In fluid-assisted metamorphic transformations, the ^{40}Ar initially
719 present in recrystallized (or dissolved) muscovite may be released in the free fluid phase,
720 locally enhancing or disrupting ^{40}Ar concentration gradients pre-existing in the original crys-
721 tals (e.g. Hames and Cheney, 1997; Scaillet, 1998; Di Vincenzo et al., 2001, 2004; Hames
722 et al., 2008; Beltrando et al., 2013; Beaudoin et al., 2020; Laurent et al., 2021). Partial to
723 complete ^{40}Ar resetting with intracrystalline ^{40}Ar/^{39}Ar gradients do exist however, as doc-
724 umented *in situ* in natural muscovite (e.g., Scaillet et al., 1990, 1992; Hames and Hodges,
725 1993; Hodges et al., 1994; Hodges and Bowring, 1995; Scaillet, 1996; Boundy et al., 1997).
726 The mere existence of these spatial gradients is indication that bulk (volume) diffusive mo-
727 tion is effectively operating in Nature, but not with the rate constants and barrier potentials
728 theoretically predicted for ideal (undefective) muscovite. The empirical Ar-Rb-Sr parallel
729 drawn above and the highly disparate ^{40}Ar diffusion rates documented both experimentally
730 and in the field clearly indicate that ^{40}Ar/^{39}Ar systematics in natural systems are not fully
731 captured yet in terms of lattice-scale processes.

732 Our findings point to a fundamental, yet largely unexplored, crystal-structural thread
733 connecting the Ar isotopic record with mixed-scale diffusional $\pm$ compositional $\pm$ struc-
734 tural *disequilibrium interactions* during the natural "growth $\rightarrow$ closure" cycle of muscovite.
735 During metamorphic $P-T$ changes, white micas react via segregation and re-organization
736 of $Si^{4+}-$rich domains involving the cooperative interdiffusion of several components such as
737 $2Na^+ + Al^{3+} = K^+ + Si^{4+} + \square$ that progressively produce discrete compositional domains dur-
738 ing re-equilibration (Shau et al., 1991), analogous to segregation of interlayer cations (Na^+,
739 Ca^{2+}, K^+) into nanodomains (Livi et al., 2008; Beltrando et al., 2013). Crystal-structural ev-
740 idence above suggests that such modifications are decoupled kinetically across the interlayer
741 hosting radiogenic ^{40}Ar, especially in the presence of grain-scale chemical potential and stress
742 gradients (Scaillet et al., 1992; Scaillet, 1996, 1998), severely impairing the interpretation of
743 microscale ^{40}Ar/^{39}Ar patterns in terms of either diffusion or (re)crystallization (Beaudoin et
744 al., 2020; Laurent et al., 2021).

745 Hence, the reason why empirical ^{40}Ar diffusion rates are so distinct from DFT and MD es-
746 timates is not failure of these approaches in describing fundamental lattice-based processes.
747 Rather, it is the manifestation of atomic-scale kinetics combining diffusion with (as yet)

27

748 largely unmodeled physics, most notably those controlling reactivity of the interlayer with
749 the external medium. Thermodynamic equilibrium is the common-denominator assumption
750 of both experimental and theoretical diffusion modeling. So far, fulfilling this condition has
751 proven elusive in the hydrothermal treatment of muscovite (Villa, 2021). In contrast, equilib-
752 rium is a built-in condition in theoretical models ensuring, as here, full control on boundary
753 conditions along with a test that the system indeed remains thermodynamically stable. As
754 such, our MD and TST diffusion estimates provide the first reliable benchmark against which
755 to gauge first-order ^{40}Ar diffusion kinetics in a stoichiometrically stable muscovite structure.
756 Combined with hydrothermal predictions (Fig. 6), they collectively define the probable $D{-}T$
757 space spanned by intracrystalline ^{40}Ar kinetics in natural muscovite. Further empirical and
758 theoretical work is required to clarify kinetic interactions between crystal-chemical disequi-
759 librium and effective ^{40}Ar diffusion across such $D{-}T$ space.

760 8. Conclusions

761 A lattice-based study of ^{40}Ar diffusion in muscovite has been attempted for the first time
762 via Molecular Dynamics simulations coupled with Nudged Elastic Band and Transition State
763 Theory. The main results lead to the following conclusions:

764

765 • ^{40}Ar diffusion in $2M_1$ muscovite predominantly occurs along the (001) interlayer with
766 recoil energies too low to permit extensive or systematic implantation of the radiogenic ^{40}Ar
767 atom more than a lattice spacing away from its production site from ^{40}K.

768

769 • Systematic energy-barrier mapping by NEB coupled with TST allows to identify the most
770 probable diffusion pathway and barrier potential for ^{40}Ar motion along the (001) interlayer;
771 ^{40}Ar transport via a divacancy mechanism is shown to be the more energetically favor-
772 able pathway for ^{40}Ar migration along (001) with characteristic diffusion parameters $E =$
773 66 kcal.mol^{-1} and $D_0 = 6 \times 10^{-4}$ cm^2.s^{-1}.

774

775 • These theoretical estimates suggest that purely diffusion-driven (Brownian) motion is not
776 an efficient mechanism for ^{40}Ar intracrystalline transport in a stoichiometrically pure and

28

777 stable muscovite structure.

778

779 • Along with hydrothermal and field-based evidence, they call for more complex (multi-scale

780 and multi-process) physics to explain ^{40}Ar exchange and retention properties of natural mus-

781 covite, most notably by considering the chemical-stoichiometric reactivity of the interlayer

782 with the external medium.

Acknowledgements

Appendix A. Supplementary Material

794 Supplementary data associated with this article can be found, in the online version, at

795 http://dx.doi.org/xx.xxx/xxxxxxxxxxxx.

References

Aagaard P. and Helgeson H. C. (1983) Activity/composition relations among silicates and aqueous solutions: II. Chemical and thermodynamic consequences of ideal mixing of atoms on homological sites in montmorillonites, illites, and mixed-layer clays. *Clays and Clay Miner.* **31**, 207-217.

Allaz, J., Engi, M., Berger, A. and Villa I. M. (2011) The effects of retrograde reactions and of diffusion on ^{40}Ar-^{39}Ar ages of micas. *J. Petrol.*, **52**, 691-716.

Althaus E., Karotke E., Nitsch K. and Winkler H. (1970) An experimental re-examination of the upper stability limit of muscovite plus quartz. *Neues Jahrb Miner. Monatsh* **7**, 325–336.

Amouric M. (1987) Growth and deformation defects in phyllosilicates as seen by HRTEM. *Acta Crystal. B* **43**, 57-63.

Argyris D., Ho T., Cole D. R. and Striolo A. (2011a) Molecular dynamics studies of interfacial water at the alumina surface. *J. Phys. Chem. C* **15**, 2038-2046.

Argyris D., Ashby P. D. and Striolo A. (2011b) Structure and orientation of interfacial water determine atomic force microscopy results: insights from molecular dynamics simulations. *ACS nano* **5**, 2215-2223.

Armstrong R. L. (1966) K-Ar dating of plutonic and volcanic rocks in orogenic belts. In *Potassium Argon dating* (eds. O.A. Schaeffer and J. Zähringer). Springer-Verlag, Berlin, p 117-133.

Arnaud N. and Kelley S. P. (1995) Evidence for excess argon during high pressure metamorphism in the Dora Maira Massif (western Alps, Italy), using an ultra-violet laser ablation microprobe ^{40}Ar–^{39}Ar technique. *Contrib. Miner. Petrol.* **121**, 1-11.

Bailey S. W. (1984) Classification and structures of the Micas. In *Micas* (ed. S.W. Bailey). Rev. Miner. **13**, 1-12.

Baldelli C., Franceschelli M., Leoni L. and Memmi I. (1989) Ferrimuscovite and celadonite substitutions in muscovite from Fe^{3+}-rich low-grade psammitic rocks (Northern Apennines, Italy).

<i>Lithos</i> **23**, 201-208.

Balogh K. and Dunkl I. (2005) Argon and fission track dating of Alpine metamorphism and basement exhumation in the Sopron Mts.(Eastern Alps, Hungary): thermochronology or mineral growth? <i>Miner. Petrol.</i> **83**, 191-218.

Balout H., Roques J., Gautheron C., Tassan-Got L. and Mbongo-Djimbi D. (2017a) Helium diffusion in pure hematite (α-Fe$_2$O$_3$) for thermochronometric applications: A theoretical multi-scale study. <i>Comput. Theor. Chem.</i> **1099**, 21-28.

Balout H., Roques J., Gautheron C. and Tassan-Got L. (2017b) Computational investigation of interstitial neon diffusion in pure hematite. <i>Comput. Mater. Sci.</i> **128**, 67-74.

Bassal F., Roques J. and Gautheron C. (2020) Neon diffusion in goethite, α-FeO(OH): a theoretical multi-scale study. <i>Phys. Chem. Miner.</i> **47**, 1-14.

Beaudoin A., Scaillet S., Mora N., Jolivet L. and Augier R. (2020) In Situ and Step-Heating ^{40}Ar/^{39}Ar Dating of White Mica in Low-Temperature Shear Zones (Tenda Massif, Alpine Corsica, France). <i>Tectonics</i> **39**, e2020TC006246.

Bell I. A. and Wilson C. (1977) Growth defects in metamorphic biotite. <i>Phys. Chem. Miner.</i> **2**, 153-169.

Bell I. A. and Wilson C. (1981) Deformation of biotite and muscovite: TEM microstructure and deformation model. <i>Tectonophysics</i> **78**, 201-228.

Beltrando M., Di Vincenzo G. and Ferraris C. (2013) Preservation of sub-microscopic structural relicts in micas from the Gran Paradiso Massif (Western Alps): Implications for ^{40}Ar–^{39}Ar geochronology. <i>Geochim. Cosmochim. Acta</i> **119**, 359-380.

Bengtson A., Ewing R. C. and Becker U. (2012) He diffusion and closure temperatures in apatite and zircon: A density functional theory investigation. <i>Geochim. Cosmochim. Acta</i> **86**, 228-238.

Blanckenburg F. v., Villa I., Baur H., Morteani G. and Steiger R. (1989) Time calibration of a PT-path from the Western Tauern Window, Eastern Alps: the problem of closure temperatures.

846   *Contrib. Miner. Petrol.* **101**, 1-11.

847 Bosse V., Féraud G., Ballèvre M., Peucat J. J. and Corsini M. (2005) Rb-Sr and $^{40}Ar/^{39}Ar$ ages
848   in blueschists from the Ile de Groix (Armorican Massif, France): Implications for closure
849   mechanisms in isotopic systems. *Chem. Geol.* **220**, 21-45.

850 Boundy T. M., Hall C. M., Li G., Essene E. J. and Halliday A. (1997) Fine-scale isotopic hetero-
851   geneities and fluids in the deep crust: a $^{40}Ar/^{39}Ar$ laser ablation and TEM study of muscovites
852   from a granulite-eclogite transition zone. *Earth Planet. Sci. Lett.* **148**, 223-242.

853 Bröcker M., Baldwin S. and Arkudas R. (2013) The geological significance of $^{40}Ar/^{39}Ar$ and Rb–Sr
854   white mica ages from Syros and Sifnos, Greece: a record of continuous (re)crystallization
855   during exhumation? *J. Metam. Geol.* **31**, 629-646.

856 Catti M., Ferraris G. and Ivaldi G. (1989) Thermal strain analysis in the crystal structure of
857   muscovite at 700 °C. *Eur. J. Mineral.*, 625-632.

858 Churakov S. V. (2013) Mobility of Na and Cs on montmorillonite surface under partially saturated
859   conditions. *Environ. sci. technol.* **47**, 9816-9823.

860 Cliff R., Bond C., Butler R. and Dixon J. (2017) Geochronological challenges posed by continuously
861   developing tectonometamorphic systems: insights from Rb/Sr mica ages from the Cycladic
862   Blueschist Belt, Syros (Greece). *J. Metam. Geol.* **35**, 197-211.

863 Cole D. R. and Chakraborty S. (2001) Rates and mechanisms of isotopic exchange. *Rev. Mineral.*
864   *Geochem.* **43**, 83-223.

865 Cosca M., Stunitz H., Bourgeix A. L. and Lee J. P. (2011) $^{40}Ar*$ loss in experimentally deformed
866   muscovite and biotite with implications for $^{40}Ar/^{39}Ar$ geochronology of naturally deformed
867   rocks. *Geochim. Cosmochim. Acta* **75**, 7759-7778.

868 Cygan R. T., Liang J. J. and Kalinichev A. G. (2004) Molecular models of hydroxide, oxyhydroxide,
869   and clay phases and the development of a general force field. *J. Phys. Chem. B* **108**, 1255-
870   1266.

Cygan R. T., Greathouse J. A., Heinz H. and Kalinichev A. G. (2009) Molecular models and simulations of layered materials. *J. Mater. Chem.* **19**, 2470-2481.

Dahl P. S. (1996) The crystal-chemical basis for Ar retention in micas: inferences from interlayer partitioning and implications for geochronology. *Contrib. Miner. Petrol.* **123**, 22-39.

Di Vincenzo G., Ghiribelli B., Giorgetti G. and Palmeri R. (2001) Evidence of a close link between petrology and isotope records: constraints from SEM, EMP, TEM and in situ ^{40}Ar-^{39}Ar laser analyses on multiple generations of white micas (Lanterman Range, Antarctica). *Earth Planet. Sci. Lett.* **192**, 389-405.

Di Vincenzo G., Carosi R. and Palmeri R. (2004) The relationship between tectono-metamorphic evolution and argon isotope records in white mica: constraints from in situ ^{40}Ar-^{39}Ar laser analysis of the Variscan basement of Sardinia. *J. Petrol.* **45**, 1013-1043.

Di Vincenzo G., Tonarini S., Lombardo B., Castelli D. and Ottolini L. (2006) Comparison of ^{40}Ar-^{39}Ar and Rb-Sr data on phengites from the UHP Brossasco–Isasca Unit (Dora Maira Massif, Italy): implications for dating white mica. *J. Petrol.* **47**, 1439-1465.

Djimbi D. M., Gautheron C., Roques J., Tassan-Got L., Gerin C. and Simoni E. (2015) Impact of apatite chemical composition on (U-Th)/He thermochronometry: An atomistic point of view. *Geochim. Cosmochim. Acta* **167**, 162-176.

Dodson M. H. (1973) Closure temperature in cooling geochronological and petrological systems. *Contrib. Miner. Petrol.* **40**, 259-274.

Domingos R., Tremblay M. M., Shuster D. L. and Militzer B. (2020) Simulations and Experiments Reveal Effect of Nanopores on Helium Diffusion in Quartz. *ACS Earth Space Chem.* **4**, 1906–1912.

Dong H., Hall C. M., Peacor D. R. and Halliday A. N. (1995) Mechanisms of argon retention in clays revealed by laser ^{40}Ar-^{39}Ar dating. *Science* **267**, 355-359.

Dunlap W. (1997) Neocrystallization or cooling? ^{40}Ar/^{39}Ar ages of white micas from low-grade mylonites. *Chem. Geol.* **143**, 181-203.

Dunlap W. and Kronenberg A. (2001) Argon loss during deformation of micas: constraints from laboratory deformation experiments. *Contrib. Miner. Petrol.* **141**, 174-185.

Elphick S. and Graham C. (1988) The effect of hydrogen on oxygen diffusion in quartz: evidence for fast proton transients? *Nature* **335**, 243–245.

Farver J. R. and Yund R. A. (1990) The effect of hydrogen, oxygen, and water fugacity on oxygen diffusion in alkali feldspar. *Geochim. Cosmochim. Acta* **54**, 2953–2964.

Ferrage E., Lanson B., Michot L. J. and Robert J.-L. (2010) Hydration properties and interlayer organization of water and ions in synthetic Na-smectite with tetrahedral layer charge. Part 1. Results from X-ray diffraction profile modeling. *J. Phys. Chem. C* **114**, 4515-4526.

Frenkel D. and Smit B. (2002) *Understanding Mol. Simul.: from algorithms to applications. Second edition.* Academic Press, San Diego.

Forster M. A. and Lister G. S. (2014) ^{40}Ar/^{39}Ar geochronology and the diffusion of ^{39}Ar in phengite–muscovite intergrowths during step-heating experiments in vacuo. *Geol. Soc., Lond., Spec. Publ.* **378**, 117–135.

Fortier S. M. and Giletti B. J. (1991) Volume self-diffusion of oxygen in biotite, muscovite, and phlogopite micas. *Geochim. Cosmochim. Acta* **55**, 1319-1330.

Gautheron C., Djimbi D. M., Roques J., Balout H., Ketcham R. A., Simoni E., Pik R., Seydoux-Guillaume A.-M. and Tassan-Got L. (2020) A multi-method, multi-scale theoretical study of He and Ne diffusion in zircon. *Geochim. Cosmochim. Acta* **268**, 348-367.

Gerin C., Gautheron C., Oliviero E., Bachelet C., Djimbi D. M., Seydoux-Guillaume A.-M., Tassan-Got L., Sarda P., Roques J. and Garrido F. (2017) Influence of vacancy damage on He diffusion in apatite, investigated at atomic to mineralogical scales. *Geochim. Cosmochim. Acta* **197**, 87-103.

Glodny J., Bingen B., Austrheim H., Molina J. F. and Rusin A. (2002) Precise eclogitization ages deduced from Rb/Sr mineral systematics: the Maksyutov complex, Southern Urals, Russia. *Geochim. Cosmochim. Acta* **66**, 1221-1235.

Glodny J., Kühn A. and Austrheim H. (2008) Geochronology of fluid-induced eclogite and amphibolite facies metamorphic reactions in a subduction-collision system, Bergen Arcs, Norway. *Contrib. Miner. Petrol.* **156**, 27-48.

Greathouse J. A. and Cygan R. T. (2005) Molecular dynamics simulation of uranyl (VI) adsorption equilibria onto an external montmorillonite surface. *Phys. Chem. Chem. Phys.* **7**, 3580-3586.

Greathouse J. A. and Cygan R. T. (2006) Water structure and aqueous uranyl (VI) adsorption equilibria onto external surfaces of beidellite, montmorillonite, and pyrophyllite: Results from Mol. Simul.s. *Environ. sci. technol.* **40**, 3865-3871.

Halama R., Konrad-Schmolke M., Sudo M., Marschall H. R. and Wiedenbeck M. (2014) Effects of fluid-rock interaction on $^{40}Ar/^{39}Ar$ geochronology in high-pressure rocks (Sesia-Lanzo Zone, Western Alps). *Geochim. Cosmochim. Acta* **126**, 475-494.

Hames W. and Bowring S. (1994) An empirical evaluation of the argon diffusion geometry in muscovite. *Earth Planet. Sci. Lett.* **124**, 161-169.

Hames W. E. and Cheney J. (1997) On the loss of $^{40}Ar*$ from muscovite during polymetamorphism. *Geochim. Cosmochim. Acta* **61**, 3863-3872.

Hames W. and Hodges K. (1993) Laser $^{40}Ar/^{39}Ar$ evaluation of slow cooling and episodic loss of ^{40}Ar from a sample of polymetamorphic muscovite. *Science* **261**, 1721-1723.

Hames W. E., Cheney J. T. and Tracy R. J. (2008) Single-crystal $^{40}Ar/^{39}Ar$ age variation in muscovite of the Gassetts Schist and associated gneiss, Vermont Appalachians. *Am. Mineral.* **93**, 384-395.

Hammouda T. and Cherniak D. (2000) Diffusion of Sr in fluorphlogopite determined by Rutherford backscattering spectrometry. *Earth Planet. Sci. Lett.* **178**, 339-349.

Harrison T. M., Célérier J., Aikman A. B., Hermann J. and Heizler M. T. (2009) Diffusion of ^{40}Ar in muscovite. *Geochim. Cosmochim. Acta* **73**, 1039-1051.

Hart S. R. (1960) Mineral ages and metamorphism. Ph. D. thesis, Massachusetts Institute of

948 Technology.

949 Helgeson H. C. and Aagaard P. (1985) Activity/composition relations among silicates and aque-
950 ous solutions; I, Thermodynamics of intrasite mixing and substitutional order/disorder in
951 minerals. *Am. J. Sci.* **285**, 769-844.

952 Herrero C., Sanz J. and Serratosa J. (1985) Si, Al distribution in micas; analysis by high-resolution
953 ^{29}Si NMR spectroscopy. *J. Phys. C* **18**, 13.

954 Herrero C., Gregorkiewitz M., Sanz J. and Serratosa J. (1987) ^{29}Si MAS-NMR spectroscopy of
955 mica-type silicates: Observed and predicted distribution of tetrahedral Al-Si. *Phys. Chem.*
956 *Miner.* **15**, 84-90.

957 Hess J., Lippolt H. and Wirth R. (1987) Interpretation of ^{40}Ar/^{39}Ar spectra of biotites: Evidence
958 from hydrothermal degassing experiments and TEM studies. *Chem. Geol. (Isotope Geo-*
959 *science section)* **66**, 137-149.

960 Hodges K. and Bowring S. (1995) ^{40}Ar/^{39}Ar thermochronology of isotopically zoned micas: Insights
961 from the southwestern USA proterozoic orogen. *Geochim. Cosmochim. Acta* **59**, 3205-3220.

962 Hodges K. V., Harries W. E. and Bowring S. A. (1994) ^{40}Ar/^{39}Ar age gradients in micas from
963 a high-temperature-low-pressure metamorphic terrain: Evidence for very slow cooling and
964 implications for the interpretation of age spectra. *Geology* **22**, 55-58.

965 Ho T. A., Argyris D., Papavassiliou D. V., Striolo A., Lee L. L. and Cole D. R. (2011) Interfacial
966 water on crystalline silica: a comparative molecular dynamics simulation study. *Mol. Simul.*
967 **37**, 172-195.

968 Itaya T., Hyodo H., Tsujimori T., Wallis S., Aoya M., Kawakami T. and Gouzu C. (2009) Regional-
969 Scale Excess Ar wave in a Barrovian type metamorphic belt, eastern Tibetan Plateau. *Island*
970 *Arc* **18**, 293-305.

971 Jónsson H., Mills G. and Jacobsen K. W. (1998) Nudged elastic band method for finding minimum
972 energy paths of transitions. In *Classical and Quantum Dynamics in Condensed Phase Sim-*
973 *ulations* (eds B. J. Berne, G. Ciccotti, and D. F. Coker). World Scientific, Singapore, pp.

385-404.

Kalinichev A. G., Padma Kumar P. and James Kirkpatrick R. (2010) Molecular dynamics computer simulations of the effects of hydrogen bonding on the properties of layered double hydroxides intercalated with organic acids. *Phil. Mag.* **90**, 2475-2488.

Kerisit S., Liu C. and Ilton E. S. (2008) Molecular dynamics simulations of the orthoclase (001)-and (010)-water interfaces. *Geochim. Cosmochim. Acta* **72**, 1481-1497.

Kirkpatrick R., Kalinichev A. and Wang J. (2005) Molecular dynamics modelling of hydrated mineral interlayers and surfaces: structure and dynamics. *Mineral. Mag.* **69**, 289-308.

Kirschner D. L., Cosca M. A., Masson H. and Hunziker J. C. (1996) Staircase $^{40}Ar/^{39}Ar$ spectra of fine-grained white mica: Timing and duration of deformation and empirical constraints on argon diffusion. *Geology* **24**, 747-750.

Kramar N., Cosca M. A. and Hunziker J. C. (2001) Heterogeneous $^{40}Ar*$ distributions in naturally deformed muscovite: in situ UV-laser ablation evidence for microstructurally controlled intragrain diffusion. *Earth Planet. Sci. Lett.* **192**, 377-388.

Kramar N., Cosca M. A., Buffat P. A. and Baumgartner L. P. (2003) Stacking fault-enhanced argon diffusion in naturally deformed muscovite. *Geol. Soc., Lond., Spec. Publ.* **220**, 249-260.

Kronenberg A. K., Kirby S. H. and Pinkston J. (1990) Basal slip and mechanical anisotropy of biotite. *J. Geophys. Res. Solid Earth* **95**, 19257-19278.

Larentzos J. P., Greathouse J. A. and Cygan R. T. (2007) An ab initio and classical molecular dynamics investigation of the structural and vibrational properties of talc and pyrophyllite. *J. Phys. Chem. C* **111**, 12752-12759.

Laurent V., Scaillet S., Jolivet L., Augier R. and Roche V. (2021) ^{40}Ar behaviour and exhumation dynamics in a subduction channel from multi-scale $^{40}Ar/^{39}Ar$ systematics in phengite. *Geochim. Cosmochim. Acta* **311**, 141-173.

Lee J. K. (1995) Multipath diffusion in geochronology. *Contrib. Miner. Petrol.* **120**, 60-82.

Lister G. S. and Baldwin S. L. (1996) Modelling the effect of arbitrary PTt histories on argon diffusion in minerals using the MacArgon program for the Apple Macintosh. *Tectonophysics* **253**, 83–109.

Lister G. and Forster M. (2016) White mica $^{40}Ar/^{39}Ar$ age spectra and the timing of multiple episodes of high-P metamorphic mineral growth in the Cycladic eclogite–blueschist belt, Syros, Aegean Sea, Greece. *J. Metam. Geol.* **34**, 401–421.

Liu H., Wang L., Li S., Yang Y., Tian H., Sun F., Liu L., Li Y., Cui Y. and others (2021) A first-principles study of helium diffusion in quartz and coesite under high pressure up to 12GPa. *Geosci. Front.* **12**, 1001-1009.

Liu X., Lu X., Wang R., Zhou H. and Xu S. (2007) Interlayer structure and dynamics of alky-lammonium-intercalated smectites with and without water: A molecular dynamics study. *Clays and Clay Miner.* **55**, 554-564.

Liu X., Lu X., Wang R. and Zhou H. (2008) Effects of layer-charge distribution on the thermody-namic and microscopic properties of Cs-smectite. *Geochim. Cosmochim. Acta* **72**, 1837-1847.

Livi K. J., Christidis G. E., Árkai P. and Veblen D. R. (2008) White mica domain formation: A model for paragonite, margarite, and muscovite formation during prograde metamorphism. *Am. Mineral.* **93**, 520-527.

Loewenstein W. (1954) The distribution of aluminum in the tetrahedra of silicates and aluminates. *Am. Mineral.: J. Earth Planet. Mater.* **39**, 92-96.

Loganathan N. and Kalinichev A. G. (2013) On the hydrogen bonding structure at the aqueous interface of ammonium-substituted mica: A molecular dynamics simulation. *Zeitschrift für Naturforschung A* **68**, 91-100.

Malani A., Ayappa K. and Murad S. (2009) Influence of hydrophilic surface specificity on the structural properties of confined water. *J. Phys. Chem. B* **113**, 13825-13839.

Massonne H. J. and Schreyer W. (1987) Phengite geobarometry based on the limiting assemblage with K-feldspar, phlogopite, and quartz. *Contrib. Miner. Petrol.* **96**, 212-224.

38

Massonne H. J. and Schreyer W. (1989) Stability field of the high-pressure assemblage, talc + phengite and two new phengite barometers. *Eur. J. Mineral.* **1**, 391-410.

McDougall I. and Harrison T. M. (1999) *Geochronology and Thermochronology by the $^{40}Ar/^{39}Ar$ Method.*, Oxford University Press, New York.

Mehrer H. (2007) *Diffusion in solids: fundamentals, methods, materials, diffusion-controlled processes.*, Springer Science & Business Media.

Meleshyn A. (2008) Two-dimensional ordering of water adsorbed on a mica surface at room temperature. *J. Phys. Chem. C* **112**, 14495-14500.

Mellini M. (1982) The crystal structure of lizardite 1T: hydrogen bonds and polytypism. *Am. Mineral.* **67**, 587-598.

Momma K. and Izumi F. (2011) VESTA 3 for three-dimensional visualization of crystal, volumetric and morphology data. *J. appl. crystal.* **44**, 1272-1276.

Monié, P. (1990) Preservation of Hercynian $^{40}Ar/^{39}Ar$ ages through high-pressure low-temperature Alpine metamorphism in the Western Alps. *Eur. J. Mineral.*, 343-361.

Monié P. and Chopin C. (1991) $^{40}Ar/^{39}Ar$ dating in coesite-bearing and associated units of the Dora Maira massif, Western Alps. *Eur. J. Mineral.*, 239-262.

Morrow C. P., Yazaydin A. Ö., Krishnan M., Bowers G. M., Kalinichev A. G. and Kirkpatrick R. J. (2013) Structure, energetics, and dynamics of smectite clay interlayer hydration: Molecular dynamics and metadynamics investigation of Na-hectorite. *J. Phys. Chem. C* **117**, 5172-5187.

Mulch A., Cosca M. and Handy M. (2002) In-situ UV-laser $^{40}Ar/^{39}Ar$ geochronology of a micaceous mylonite: an example of defect-enhanced argon loss. *Contrib. Miner. Petrol.* **142**, 738-752.

Padma Kumar P., Kalinichev A. G. and Kirkpatrick R. J. (2006) Hydration, swelling, interlayer structure, and hydrogen bonding in organolayered double hydroxides: Insights from molecular dynamics simulation of citrate-intercalated hydrotalcite. *J. Phys. Chem. B* **110**, 3841-3844.

Purdy J. and Jäger E. (1976) K-Ar ages on rock forming minerals from the Central Alps. *Mem. 1st. Geol. Min. Univ. Padova* **30**, 31.

Putlitz B., Cosca M. and Schumacher J. (2005) Prograde mica $^{40}Ar/^{39}Ar$ growth ages recorded in high pressure rocks (Syros, Cyclades, Greece). *Chem. Geol.* **214**, 79-98.

Putnis A. (2009) Mineral replacement reactions. *Rev. Mineral. Geochem.* **70**, 87-124.

Rapaport D. C. (2004) *The art of molecular dynamics simulation.*, Cambridge university press.

Robbins C. (1972) Radiogenic argon diffusion in muscovite under hydrothermal conditions. M.S. Thesis, Brown University, Providence, RI.

Ruiz Pestana L., Kolluri K., Head-Gordon T. and Lammers L. N. (2017) Direct exchange mechanism for interlayer ions in non-swelling clays. *Environ. sci. technol.* **51**, 393-400.

Saadoune I., Purton J. A. and de Leeuw N. H. (2009) He incorporation and diffusion pathways in pure and defective zircon $ZrSiO_4$: A density functional theory study. *Chem. Geol.* **258**, 182-196.

Scaillet S. (1996) Excess ^{40}Ar transport scale and mechanism in high-pressure phengites: A case study from an eclogitized metabasite of the Dora-Maira nappe, western Alps. *Geochim. Cosmochim. Acta* **60**, 1075-1090.

Scaillet S. (1998) K-Ar ($^{40}Ar/^{39}Ar$) geochronology of ultrahigh pressure rocks. In *When continents collide: Geodynamics and geochemistry of ultrahigh-pressure rocks.* Springer. pp. 161-201.

Scaillet S., Féraud G., Lagabrielle Y., Ballèvre M. and Ruffet G. (1990) $^{40}Ar/^{39}Ar$ laser-probe dating by step heating and spot fusion of phengites from the Dora Maira nappe of the Western Alps, Italy. *Geology* **18**, 741-744.

Scaillet S., Féraud G., Ballèvre M. and Amouric M. (1992) Mg/Fe and [(Mg,Fe)Si-Al$_2$] compositional control on argon behaviour in high-pressure white micas: A $^{40}Ar/^{39}Ar$ continuous laser-probe study from the Dora-Maira nappe of the internal Western Alps, Italy. *Geochim. Cosmochim. Acta* **56**, 2851-2872.

Schertl H. P. and Hammerschmidt K. (2016) Tracking the incidence of excess argon in white mica Ar-Ar data from UHP conditions to upper crustal levels in the Dora-Maira Massif, Western Alps. *Eur. J. Mineral.* **28**, 1255-1275.

Scibiorski E., Jourdan F., Mezger K., Tohver E. and Vollstaedt H. (2021) Cryptic excess argon in metamorphic biotite: Anomalously old $^{40}Ar/^{39}Ar$ plateau dates tested with Rb/Sr thermochronology and Ar diffusion modelling. *Geochim. Cosmochim. Acta* **315**, 1–23.

Shau Y.-H., Feather M. E., Essene E. J. and Peacor D. R. (1991) Genesis and solvus relations of submicroscopically intergrown paragonite and phengite in a blueschist from northern California. *Contrib. Miner. Petrol.* **106**, 367-378.

Shea W. T. and Kronenberg A. K. (1992) Rheology and deformation mechanisms of an isotropic mica schist. *J. Geophys. Res. Solid Earth* **97**, 15201-15237.

Spencer K., Hacker B., Kylander-Clark A., Andersen T., Cottle J., Stearns M., Poletti J. and Seward G. (2013) Campaign-style titanite U-Pb dating by laser-ablation ICP: Implications for crustal flow, phase transformations and titanite closure. *Chem. Geol.* **341**, 84-101.

Szczerba M., Derkowski A., Kalinichev A. G. and Środoń J. (2015) Molecular modeling of the effects of ^{40}Ar recoil in illite particles on their K-Ar isotope dating. *Geochim. Cosmochim. Acta* **159**, 162-176.

Tao L., Xiao-Feng T., Yu Z. and Tao G. (2010) Swelling of K^+, Na^+ and Ca^{2+}-montmorillonites and hydration of interlayer cations: a molecular dynamics simulation. *Chin. Phys. B* **19**, 109101.

Tardy Y. and Fritz B. (1981) An ideal solid solution model for calculating solubility of Clay miner.. *Clay miner.* **16**, 361-373.

Teich-McGoldrick S. L., Greathouse J. A. and Cygan R. T. (2012) Molecular dynamics simulations of structural and mechanical properties of muscovite: pressure and temperature effects. *J. Phys. Chem. C* **116**, 15099-15107.

Thompson A. P., Aktulga H. M., Berger R., Bolintineanu D. S., Brown W. M., Crozier P. S.,

in 't Veld P. J., Kohlmeyer A., Moore S. G., Nguyen T. D. and others (2021) LAMMPS − a flexible simulation tool for particle-based materials modeling at the atomic, meso, and continuum scales. *Comput. Phys. Com.* **271**, 108171.

Villa I. M. (2021) The in vacuo release of Ar from minerals: 1. Hydrous minerals. *Chem. Geol.* **564**, 120076.

Villa I. M. and Puxeddu M. (1994) Geochronology of the Larderello geothermal field: new data and the "closure temperature" issue. *Contrib. Miner. Petrol.* **115**, 415-426.

Vineyard G. H. (1957) Frequency factors and isotope effects in solid state rate processes. *J. Phys. Chem. Sol.* **3**, 121-127.

Wander M. C. and Clark A. E. (2008) Structural and dielectric properties of quartz- water interfaces. *J. Phys. Chem. C* **112**, 19986-19994.

Wang G. F. and Banno S. (1987) Non-stoichiometry of interlayer cations in micas from low-to middle-grade metamorphic rocks in the Ryoke and the Sanbagawa belts, Japan. *Contrib. Miner. Petrol.* **97**, 313-319.

Wang K., Brodholt J. and Lu X. (2015) Helium diffusion in olivine based on first principles calculations. *Geochim. Cosmochim. Acta* **156**, 145-153.

Wang K., Lu X. and Brodholt J. P. (2020) Diffusion of noble gases in subduction zone hydrous minerals. *Geochim. Cosmochim. Acta* **291**, 50-61.

White, J. A. (1999) Lennard-Jones as a model for argon and test of extended renormalization group calculations. *J. Chem. Phys.* **111(20)**, 9352-9356.

Wijbrans J. R. and McDougall I. (1986) $^{40}Ar/^{39}Ar$ dating of white micas from an Alpine high-pressure metamorphic belt on Naxos (Greece): the resetting of the argon isotopic system. *Contrib. Miner. Petrol.* **93**, 187–194.

Wijbrans J. and McDougall I. (1988) Metamorphic evolution of the Attic Cycladic Metamorphic Belt on Naxos (Cyclades, Greece) utilizing $^{40}Ar/^{39}Ar$ age spectrum measurements. *J. Metam.*

1126   *Geol.* **6**, 571–594.

1127 Wunder B. and Melzer S. (2002) Interlayer vacancy characterization of synthetic phlogopitic micas
1128   by IR spectroscopy. *Eur. J. Mineral.* **14**, 1129-1138.

1129 Yu C. J., Choe S. H., Jang Y. M., Jang G. H. and Pae Y. H. (2016) First-principles study of
1130   organically modified muscovite mica with ammonium (NH_4^+) or methylammonium ($CH_3NH_3^+$)
1131   ion. *J. Mater. Sci.* **51**, 10806-10818.

1132 **Tables**

Table 1: Interaction parameters used in the simulations

Nonbonded parameters			
Atoms	Charge (e)	σ (Å)	ϵ (kcal.mol^{-1})
H (hydroxyl)[a]	0.4250	-	-
O1 (hydroxyl)[a]	-0.9500	3.1655	0.1554
O2 (bridging Oxygen)[a]	-1.0500	3.1655	0.1554
O3 (Oxygen bonded to tetrahedral Al)[a]	-1.1688	3.1655	0.1554
Al (octahedral)[a]	1.5750	4.2712	1.3298×10^{-6}
Al2 (tetrahedral)[a]	1.5750	3.3020	1.8405×10^{-6}
Si[a]	2.1000	3.3020	1.8405×10^{-6}
K[a]	1.0000	3.3340	0.1000
Ar[b]	0.0000	3.4010	0.2304

[a]Cygan et al. (2004) [b]White (1999)

Bonded parameters			
Atom 1	Atom 2	k_1 (kcal.mol^{-1}.Å^{-2})	r_0 (Å)
O1 (hydroxyl)	H (hydroxyl)	554.1349	1.0000

44

Table 2: Comparison of experimental and simulated crystallographic parameters of $2M_1$ Muscovite

	Experiment	MD simulations (CLAYFF)	Deviation ($\pm$ %)
a (Å)	5.191	5.182	-0.17
b (Å)	9.006	8.944	-0.69
c (Å)	20.068	19.697	-1.85
α (°)	90.000	89.787	-0.24
β (°)	95.770	95.936	+0.17
γ (°)	90.000	90.175	+0.19
Interlayer sep. (Å)	3.396	3.368	-0.88

Table 3: Computed migration barriers and ^{40}Ar diffusion parameters for the monovacancy ($\square$) and divacancy ($\square\square$) mechanisms.

	Mean energy barriers		Effective energy barriers		^{40}Ar Diffusion parameters	
	$\langle E^{\mathrm{Ar}}\rangle$	$\langle E^{\mathrm{K}}\rangle$	$E_{\mathrm{eff}}^{\mathrm{Ar}}$	$E_{\mathrm{eff}}^{\mathrm{K}}$	E	D_0
	(kcal.mol^{-1})	(kcal.mol^{-1})	(kcal.mol^{-1})	(kcal.mol^{-1})	(kcal.mol^{-1})	(cm^2.s^{-1})
$\square$	71 $\pm$ 5	79 $\pm$ 9	69	75	75	4×10^{-3}
$\square\square$	69 $\pm$ 6	66 $\pm$ 10	65	58	66	6×10^{-4}

Figure captions

Fig. 1. The crystal structure atomic model of muscovite imaged with VESTA (Momma and Izumi, 2011). The system ($n = 1512$ atoms) consists of a supercell ($6 \times 3 \times 1$ unit cells) of initial dimensions $L_x = 31.146$ Å, $L_y = 27.018$ Å and $L_z = 19.966$ Å. a) Perspective view down the a axis. b) Tetrahedral layers (as labelled in (a)) showing the irregular distribution of Al atoms. Atoms are drawn with their Van der Waals radii. T_{up} and T_{low} indicate the upper and the lower tetrahedral layers with respect to the interlayer region, respectively.

Fig. 2. Variation of the energy of the system during ^{40}Ar recoil with respect to the mean energy of a system in which ^{40}Ar occupies an regular interlayer site. The red line is the running mean energy averaged over 2.5 ps. The decrease of the energy at 50 ps corresponds to the move of ^{40}Ar from the interstitial site to the lattice stable site.

Fig. 3. Geometry of diffusion in the muscovite interlayer plane. a) Monovacancy mechanism. b) Divacancy mechanism. Orange and green circles correspond to K^+ and ^{40}Ar atoms respectively. $\square$ represents the vacancy, $\overrightarrow{V_i}$ are the displacement vectors and $\overrightarrow{\delta_i}$ indicate atomic jumps preserving the divacancy. See text for discussion.

Fig. 4. Results of NEB calculations of ^{40}Ar migration in muscovite. a) Histogram of migration barriers associated with a monovacancy mechanism. b) Histogram of migration barriers associated with a divacancy mechanism. c) Variation of the potential energy of ^{40}Ar along its path towards a monovacancy (black) and towards a vacancy pair (blue). d) Trajectories followed by ^{40}Ar as it migrates from a stable site towards a single vacancy (black) and towards a vacancy pair (blue). Red circles represent basal oxygens. e) Diagram showing the anticorrelation between the ^{40}Ar migration barriers and the total electrostatic energy of the structure.

Fig. 5. Results of NEB calculations of K^+ migration in muscovite. a) Histogram of migration barriers associated with a monovacancy mechanism. b) Histogram of migration barri-

1163 ers associated with a divacancy mechanism. c) Variation of the potential energy of K^+

1164 along its path towards a monovacancy (black) and towards a vacancy pair (blue). d)

1165 Trajectories followed by K^+ as it migrates from a stable site towards a single vacancy

1166 (black) and towards a vacancy pair (blue). Red circles represent basal oxygens. e)

1167 Diagram showing the positive correlation between the ^{40}Ar and K^+ migration barriers.

1168

1169 Fig. 6. Arrhenius plot of ^{40}Ar diffusion coefficients calculated for the monovacancy and the

1170 divacancy mechanisms. Results of previous studies are also reported for comparison.

1171

1172 Fig. 7. Nominal variations in ^{40}Ar−muscovite closure temperature (Eq (1) in text) with

1173 cooling rate and grain size. T_c are calculated for a cylindrical geometry ($A = 27$), using

1174 diffusion parameters deduced from Molecular Dynamics and Transition State Theory

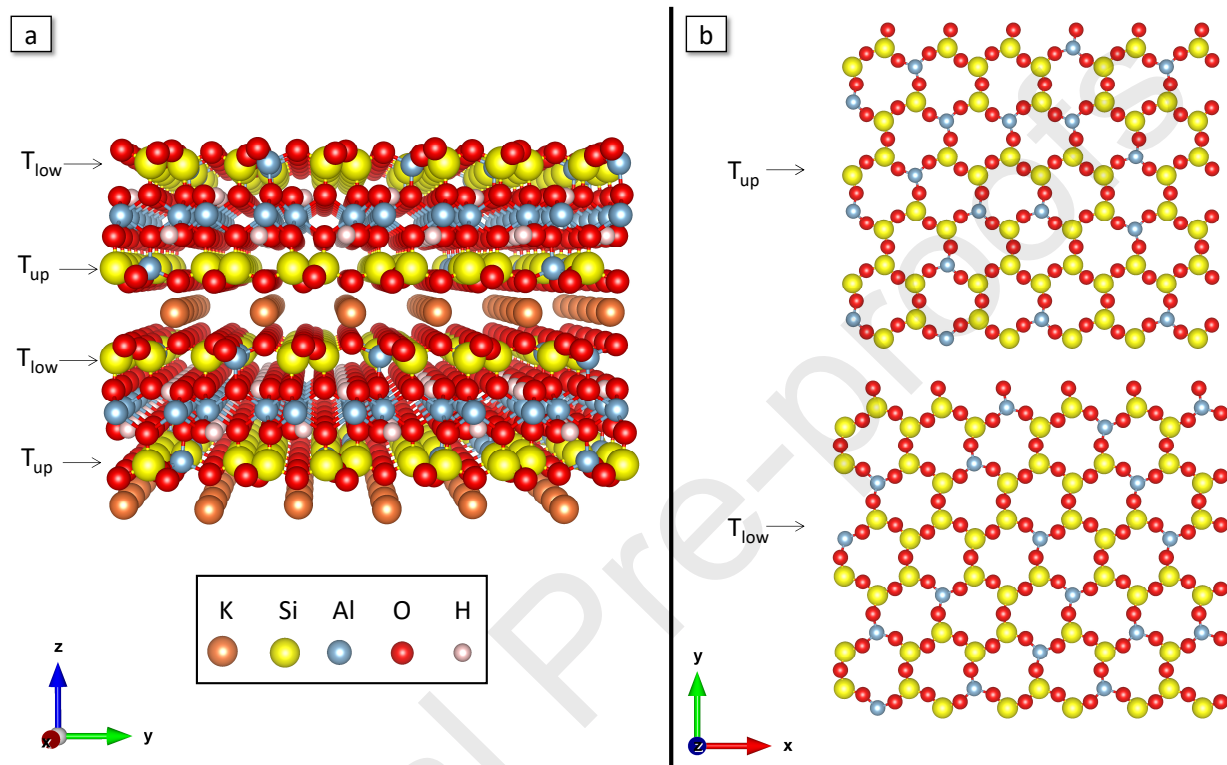1175 ($E = 66$ kcal.mol^{-1}; $D_0 = 6 \times 10^{-4}$ cm^2.s^{-1}). See text for discussion.

1176

Fig. 1

Fig. 2

Fig. 3

Fig. 4
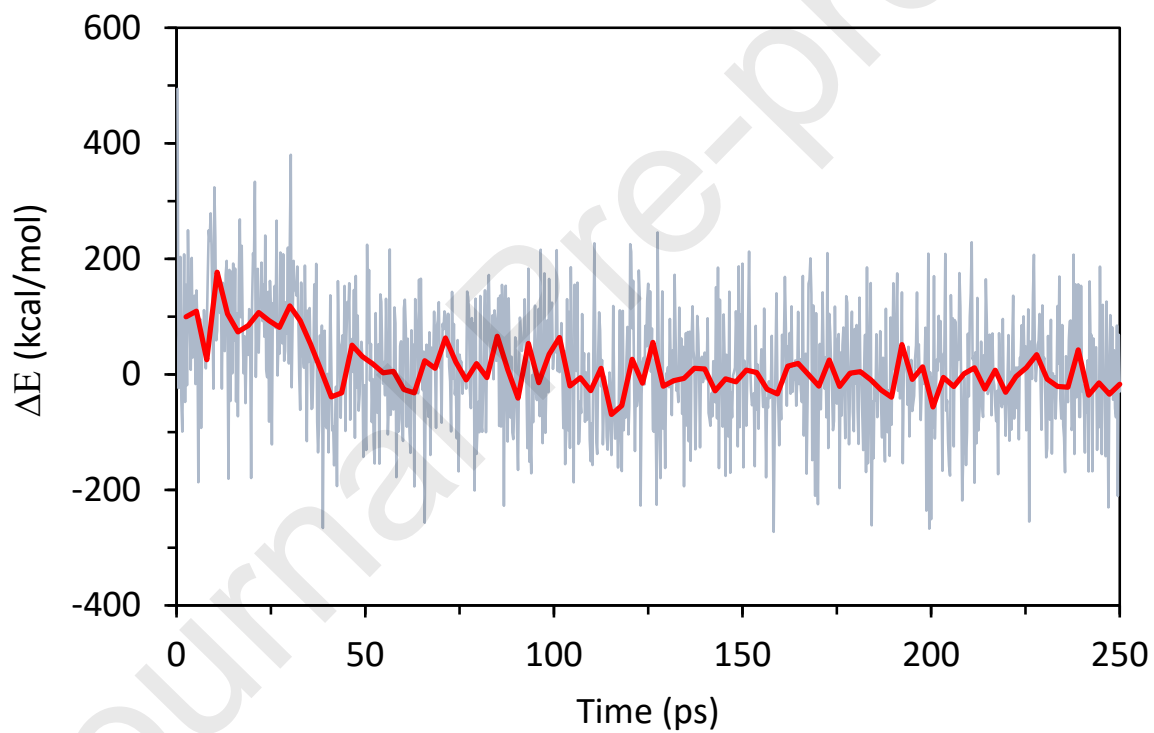
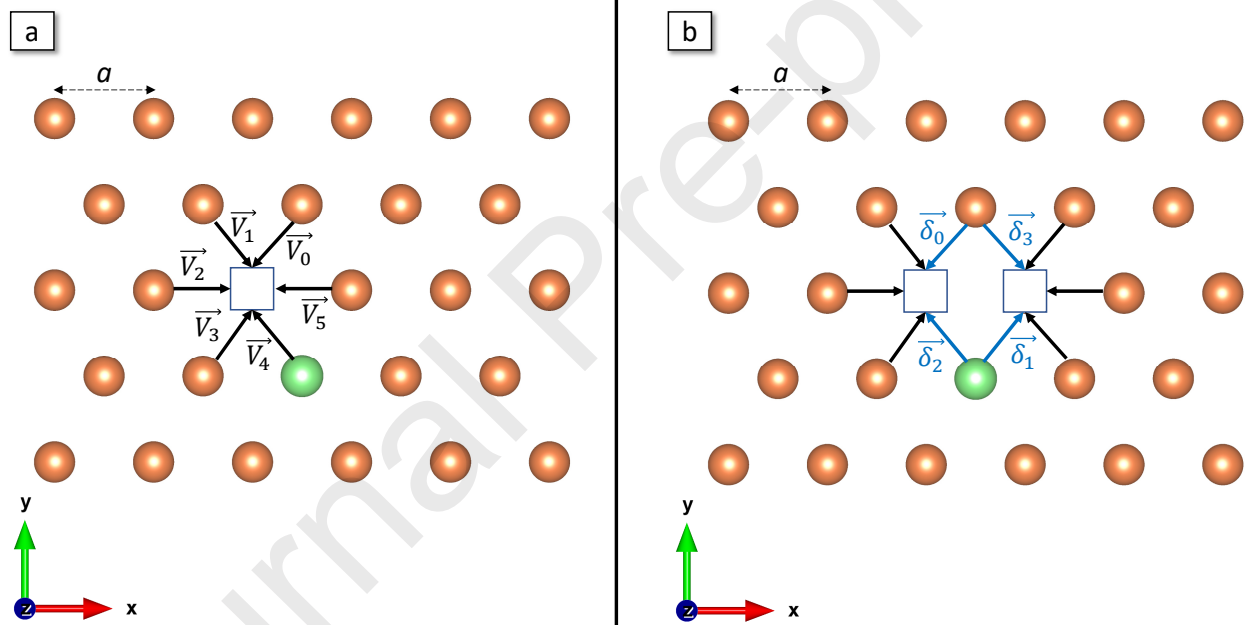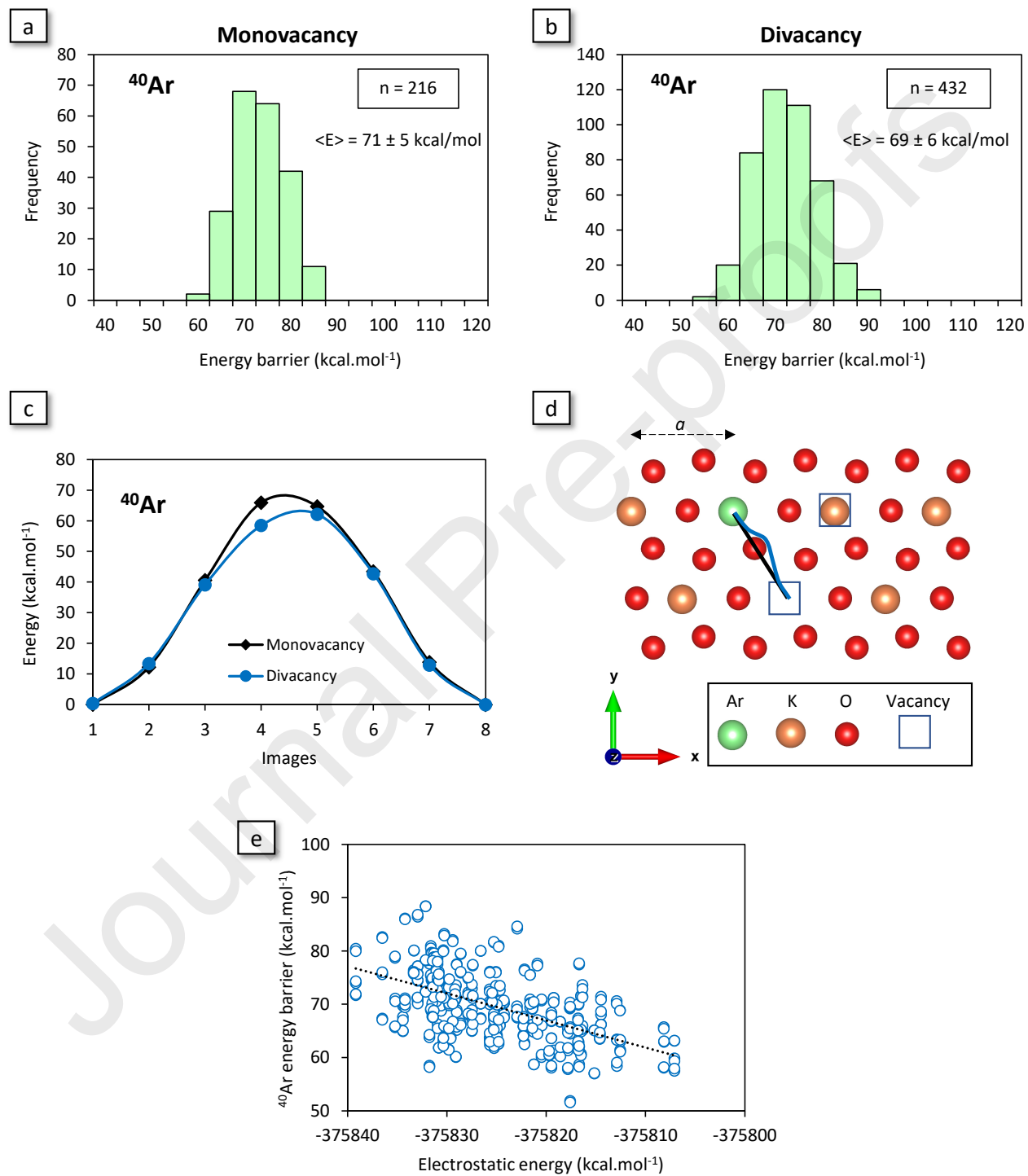Fig. 5

a

Monovacancy

K⁺

n = 216

<E> = 79 ± 9 kcal/mol

Frequency (y-axis: 0, 10, 20, 30, 40, 50, 60, 70)
Energy barrier (kcal.mol⁻¹) (x-axis: 40, 50, 60, 70, 80, 90, 100, 110, 120)

b

Divacancy

K⁺

n = 432

<E> = 66 ± 10 kcal/mol

Frequency (y-axis: 0, 20, 40, 60, 80, 100)
Energy barrier (kcal.mol⁻¹) (x-axis: 40, 50, 60, 70, 80, 90, 100, 110, 120)

c

K⁺

Energy (kcal.mol⁻¹) (y-axis: 0, 10, 20, 30, 40, 50, 60, 70, 80)
Images (x-axis: 1, 2, 3, 4, 5, 6, 7, 8)

Monovacancy
Divacancy

d

a

y
z
x

K   O   Vacancy

e

⁴⁰Ar energy barrier (kcal.mol⁻¹) (y-axis: 50, 60, 70, 80, 90, 100)
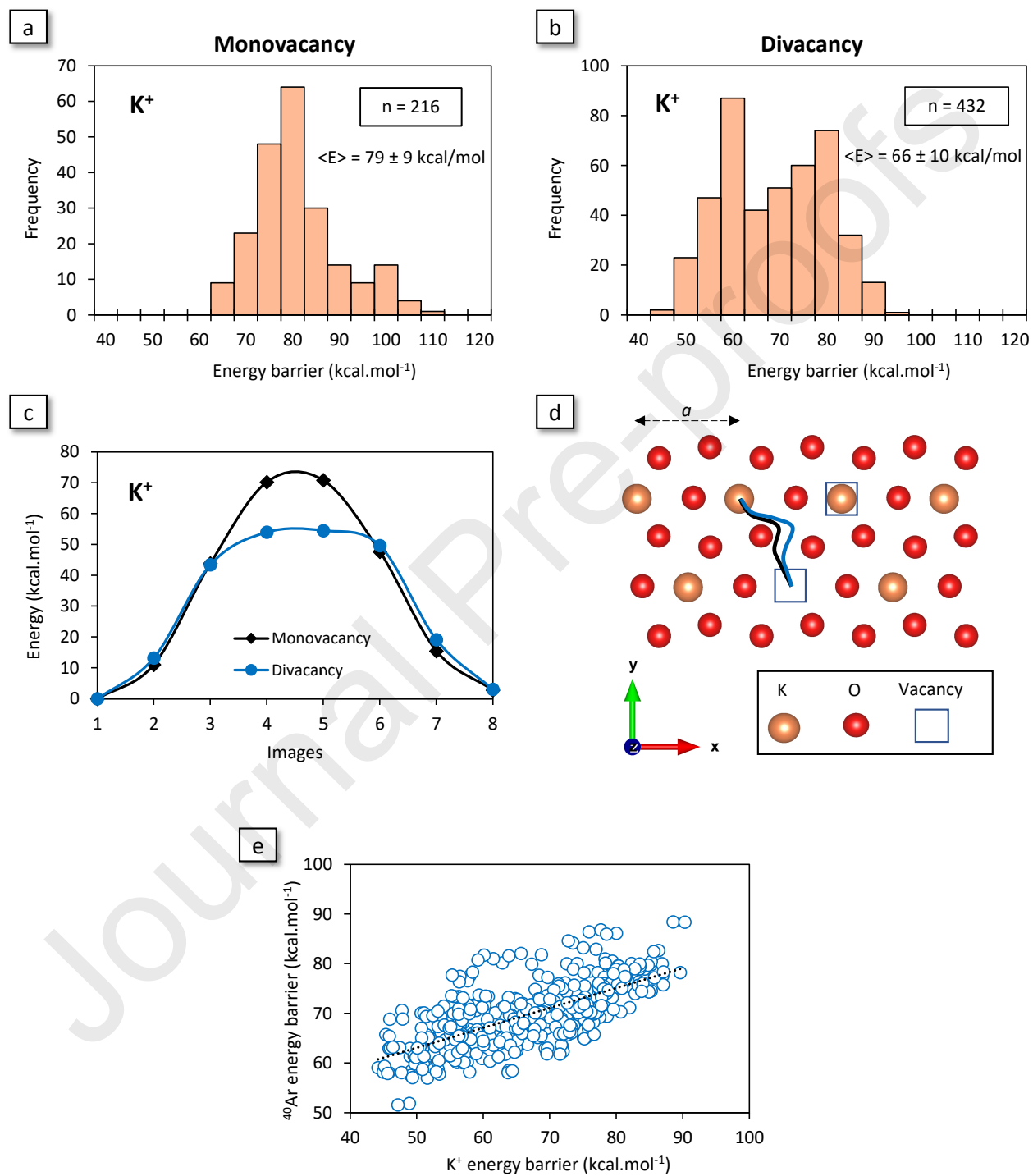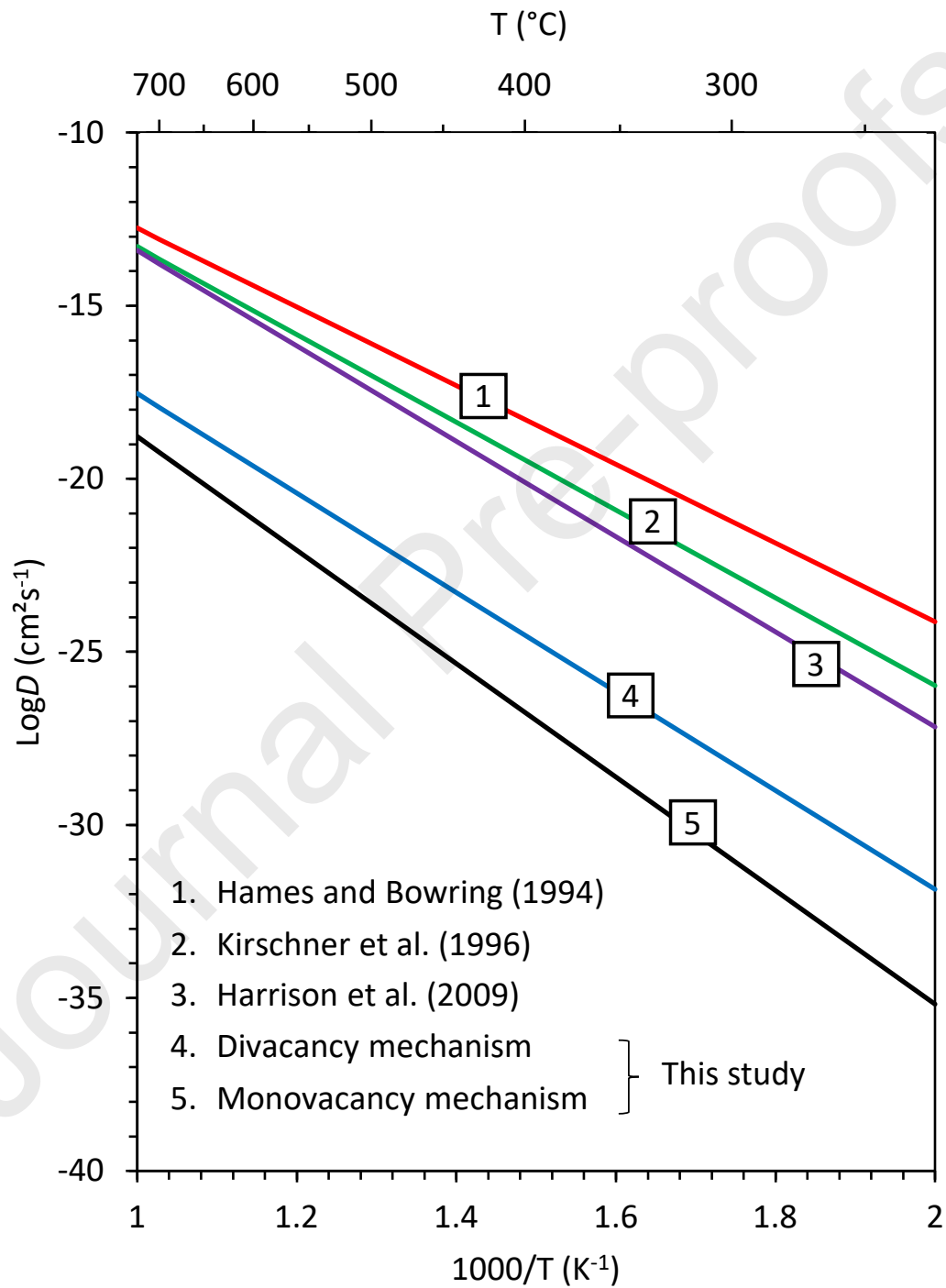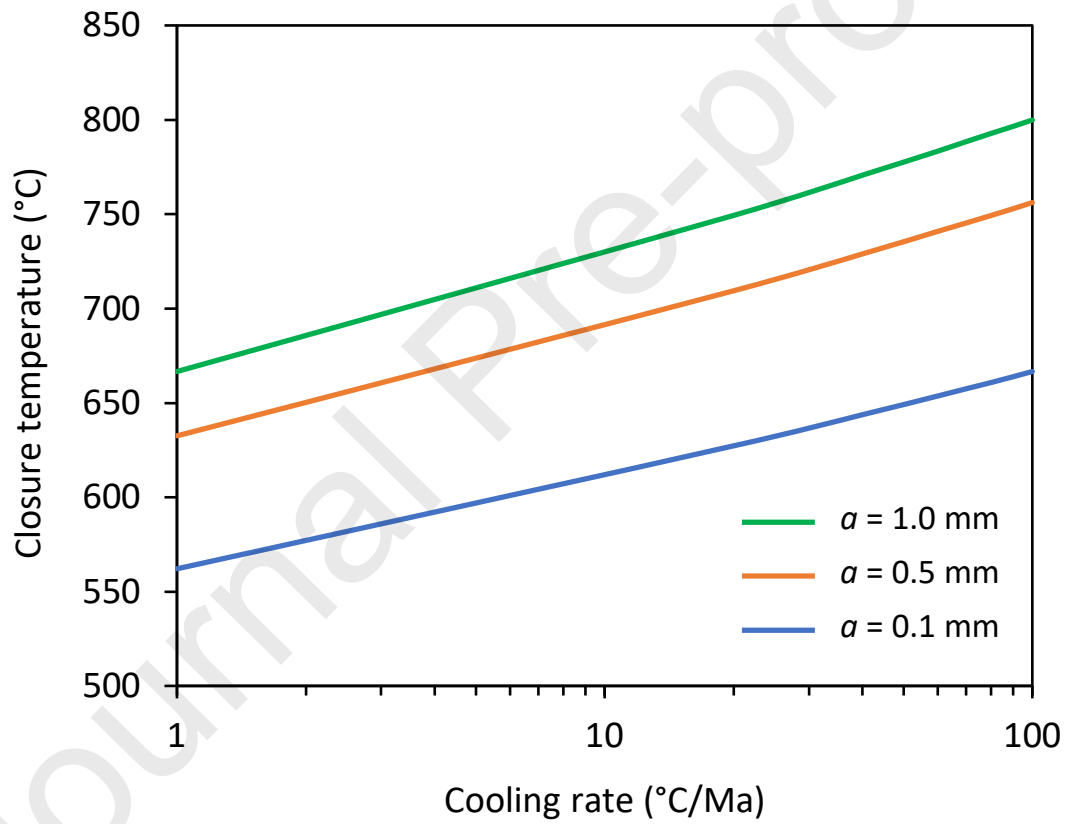K⁺ energy barrier (kcal.mol⁻¹) (x-axis: 40, 50, 60, 70, 80, 90, 100)

Fig. 6

Fig. 7

Declaration of interests

☒ The authors declare that they have no known competing financial interests or personal relationships that could have appeared to influence the work reported in this paper.

☐The authors declare the following financial interests/personal relationships which may be considered as potential competing interests: